Active and Nonlinear Wave Propagation Devices in Ultrafast Electronics and Optoelectronics

MARK J. W. RODWELL, MEMBER, IEEE, SCOTT T. ALLEN, RUAI Y. YU, MICHAEL G. CASE, UDDALAK BHATTACHARYA, MADHUKAR REDDY, ERIC CARMAN, MASAYUKI KAMEGAWA, YOSHIYUKI KONISHI, JOE PUSL, AND RAJASEKHAR PULLELA

Invited Paper

We describe active and nonlinear wave propagation devices for generation and detection of (sub)millimeter wave and (sub)picosecond signals. Shock-wave nonlinear transmission lines (NLTL's) generate ~4-V step functions with less than 0.7-ps fall times. NLTL-gated sampling circuits for signal measurement have attained over 700-GHz bandwidth. Soliton propagation on NLTL's is used for picosecond impulse generation and broadband millimeter-wave frequency multiplication. Picosecond pulses can also be generated on traveling-wave structures loaded by resonant tunneling diodes. Applications include integration of photodetectors with sampling circuits for picosecond optical waveform measurements and instrumentation for millimeter-wave waveform and network (circuit) measurements both on-wafer and in free space. General properties of linear and nonlinear distributed devices and circuits are reviewed, including gain–bandwidth limits, dispersive and nondispersive propagation, shock-wave formation, and soliton propagation.

M. J. W. Rodwell, S. T. Allen, U. Bhattacharya, M. Reddy, and R. Pullela are with the Department of Electrical and Computer Engineering, University of California, Santa Barbara, CA 93106 USA.

R. Y. Yu was with the Department of Electrical and Computer Engineering, University of California, Santa Barbara, CA 93106 USA. He is now with Rockwell International Science Center, Thousand Oaks, CA 91358 USA.

M. G. Case was with the Department of Electrical and Computer Engineering, University of California, Santa Barbara, CA 93106 USA. He is now with Hughes Aircraft Company Research Laboratories, Malibu, CA USA.

E. Carman was with the Department of Electrical and Computer Engineering, University of California, Santa Barbara, CA 93106 USA. He is now with Advanced Custom Technologies Group, Motorola Corp., Mesa, AZ USA.

M. Kamegawa and Y. Konishi were with the Department of Electrical and Computer Engineering, University of California, Santa Barbara, CA 93106 USA, on leave from Shimadzu Corporation, Kyoto, Japan.

J. Pusl was with the Department of Electrical and Computer Engineering, University of California, Santa Barbara, CA 93106 USA. He is now with Hughes Aircraft Company, Space and Communications Division, Los Angeles CA 90009 USA.

IEEE Log Number 9401513.

I. INTRODUCTION

Information transmission rates and operating frequencies of electronic systems have increased dramatically since the birth of electrical telegraphy in the 1830's [1]. Communication links have progressed from Morse code transmitted at a few symbols per second on wire pairs, through telephone (~4 kHz) voice transmission (1876), culminating in fiber-optic transmission systems carrying 150 000 conversations (10-Gb/s data rate) [2].

Broadcast frequencies have progressed from the ~800 kHz of Marconi's 1901 trans-Atlantic experiments [3], through ~500 kHz amplitude-modulation radio broadcasts (*circa* 1920) [4], ~100 MHz frequency-modulation radio (*circa* 1940) [5], to 12-GHz direct-broadcast satellite television. Early World War II radar systems operated at 23 MHz [6]; some modern radar systems use 94 GHz.

Applications at yet higher frequencies will emerge; several significant opportunities are listed. Radar is used in aviation for foul-weather runway imaging and for flying at night; increasing radar frequencies to beyond 100 GHz will increase the resolution and decrease the required antenna size. Demand for communications capacity is driven by growing use of computers, cable television, portable telephones, and facsimile machines; advances in high-speed electronics will permit 100-Gb/s data transmission on optical fibers and gigabit per second transmission on millimeter-wave radio links. Gases involved in ozone depletion in the Earth's upper atmosphere exhibit emission resonances in the 300 GHz–3 THz range; these will be monitored by satellite-based heterodyne receivers to be launched later this decade [7]. If the technology is available and inexpensive, these and other applications will arise.

Research in ultrafast electronics and optoelectronics explores the limits of high-frequency technologies. Objectives include generation and detection of transient electrical signals having risetimes of 0.1–5 ps and sinusoidal signals having frequencies from 100 GHz to several terahertz. Distributed (wave propagation) devices play a significant

role in broadband circuits, pulse generation, and instrumentation.

Most radio and radar signals are narrowband, with the information or modulation bandwidth being only a small fraction of the carrier frequency. In contrast, the pulse-code-modulation signal transmitted by a 100-Gb/s fiber-optic transmission link will have significant power over a ~1-MHz to 100-GHz bandwidth. Oscilloscopes and other instrumentation must be similarly broadband.

Narrowband systems operate at higher frequencies than pulsed or broadband systems. Resonant impedance-matching networks provide efficient coupling to semi-conductor devices over narrow bandwidths, but cannot be used where broad bandwidths or pulsed signals are required. Distributed circuits permit efficient coupling to semiconductor devices over broad bandwidths.

Schottky diodes, the fastest of semiconductor devices, are readily used for generation and detection of sinusoidal signals at submillimeter-wave frequencies [8]. Until recently, it was not clear how to use Schottky diodes for pulse generation and detection, and the rise times of electronic pulse generators were almost 100 times longer than the periods of the highest frequency electronic oscillators. Through nonlinear wave propagation, Schottky diodes *can* be used for pulse generation, with performance limited by the (multiterahertz) diode cutoff frequencies. Linear and nonlinear distributed interactions are used widely in optics, in lasers [10] (distributed gain), second-harmonic generators, and optical parametric oscillators [11].

We describe active and nonlinear electrical wave propagation devices for generation and detection of picosecond and subpicosecond electrical signals [9]. This work, development of monolithic devices, draws heavily on earlier work by Landauer [12], [13], Scott [14], Hirota [15], and others [16], [17], a field reviewed in 1970 by Scott in *Active and Nonlinear Wave Propagation in Electronics* [18]. Applications, demonstrated and potential, include millimeter-wave generation [19], instrumentation with several hundred gigahertz bandwidth [20]–[25], and multiplexers for 100-Gb/s fiber-optic transmission.

II. HIGH-FREQUENCY ELECTRONICS AND OPTOELECTRONICS

The shortest electrical pulses reported have been generated by optical–electrical conversion of subpicosecond optical pulses from pulsed lasers [10], [26], but applications have been limited by the lasers' size and complexity. The pulsed laser illuminates a photoconductor (Fig. 1), a gap between two ohmic contacts on a semiconductor, generating electron–hole pairs which increase the gap conductance $G(t)$ in proportion to the laser intensity. The photoconductor is connected to transmission lines and a bias voltage applied (Fig. 1(b)). For small illumination intensities, the output voltage is proportional to the optical power, while for high intensities the gap resistance becomes small and the photoconductor is a laser-gated switch. The impulse response duration is determined by the gap capacitance and
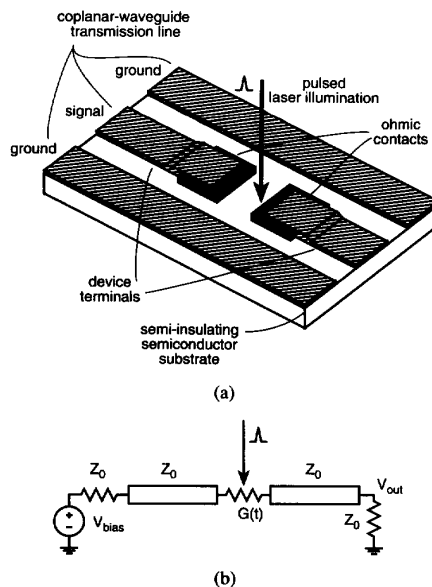

Fig. 1. Photoconductive detector connected to a coplanar-waveguide transmission line (a) for subpicosecond electrical pulse generation and sampling, and photoconductive pulse generation circuit (b).
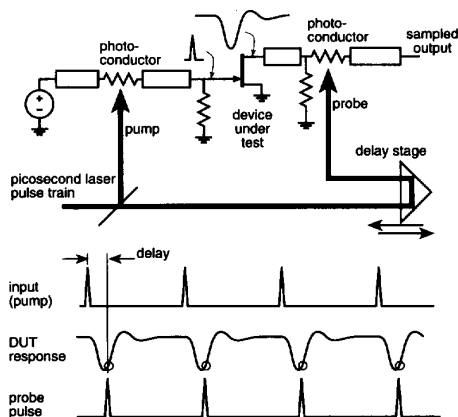

Fig. 2. Pump-probe experiments; a photoconductor generates asubpicosecond impulse driving a device under test, while a second photoconductor samples the resulting output signal.

by the carrier recombination lifetime, the latter minimized through ion implantation [27] or low-temperature growth [28].

Photoconductors are also used for signal measurement (Fig. 2) [27]. A laser-illuminated photoconductor generates a train of impulses, driving the device under test. A second photoconductor operates as a laser-gated switch, generating a sampled (dc) voltage proportional to the device output at the time of arrival of the optical pulse. Adjusting an optical delay stage varies the sampling pulse arrival time, producing a measurement of the device output-voltage waveform as a function of time. Comparing the Fourier spectra of the incident and transmitted pulses, transmission-frequency measurements of materials or devices are made.

Photoconductors integrated with on-wafer broadband antennas are used to generate and radiate, then receive and sample, subpicosecond electromagnetic pulses; by passing the radiation through test samples, material absorption spectra have been measured at low terahertz frequencies [29].

Subpicosecond electrical transients are also measured by electrooptic sampling [30]. Both lithium niobate and III–V compound semiconductors exhibit small anisotropic variations in their optical refractive indices in response to applied electric fields [11]. Electric fields associated with nearby conductors can be measured by measuring the change in polarization of an optical pulse passing through the crystal. As with photoconductive sampling (Fig. 2), electrooptic sampling measures electrical waveforms by using pairs of synchronized optical pulses for signal generation (using a photoconductor) and electrooptic signal measurement. Using electrooptic sampling, Keil has measured 150-fs risetime step functions [26].

Our objective is to explore a similar domain with solid-state devices. Presently, transistors have insufficient bandwidth for submillimeter wave or subpicosecond pulse generation. High-electron-mobility field-effect-transistors (HEMT's) with power–gain cutoff frequencies ($f_{\max}$) above 450 GHz have been reported [31], [32]. A monolithic resonant-matched HEMT amplifier [33] has attained 6 dB per stage gain over a narrow 112–115-GHz bandwidth, while a monolithic HEMT *distributed* amplifier [34] has attained 5-dB gain over a broad 5–100-GHz bandwidth. Given the 100-GHz bandwidth, this distributed amplifier must have a step-response rise time of 3–4 ps; shorter step-response rise times require an increase in transistor $f_{\max}$.

Diodes are used for signal generation and detection at frequencies well above transistor bandwidths. Schottky diodes have RC cutoff frequencies $f_c = 1/2\pi r_s C_d$ in the infrared, where r_s is the diode parasitic series resistance and C_d the depletion capacitance. Under forward bias, a diode is a nonlinear conductance, with the forward current I varying with the applied voltage V as $I \propto \exp(qV/kT)$, where q is the electron charge, k is Boltzmann's constant, and T is the temperature (Fig. 3(a)). Under reverse bias, the diode is a nonlinear charge-storage element (Fig. 3(b)), with the charge varying as $Q(V) \propto \sqrt{\phi - V}$ for a uniformly doped diode, where $\phi \cong 0.8$ V is the barrier potential for GaAs. In either case, the diode will generate harmonics and difference frequencies of applied signals. Combined with matching and frequency-selection networks, diodes are used for both mixing (Fig. 3(c)) and harmonic generation (Fig. 3(d)).

Crowe has reported Schottky diodes with $f_c = 25$ THz [8]. Röser [35] has reported a 2.5-THz mixer with 25 000 K noise temperature. Rothermel [36] has reported a Schottky-diode frequency multiplier with 800-GHz output. Resonant tunneling diodes (RTD's) have oscillated at 712 GHz [37]. Schottky diode operating frequencies are comparable to the signal bandwidths generated by photoconductors, but the circuits (Fig. 3(c), (d)) are frequency-selective and
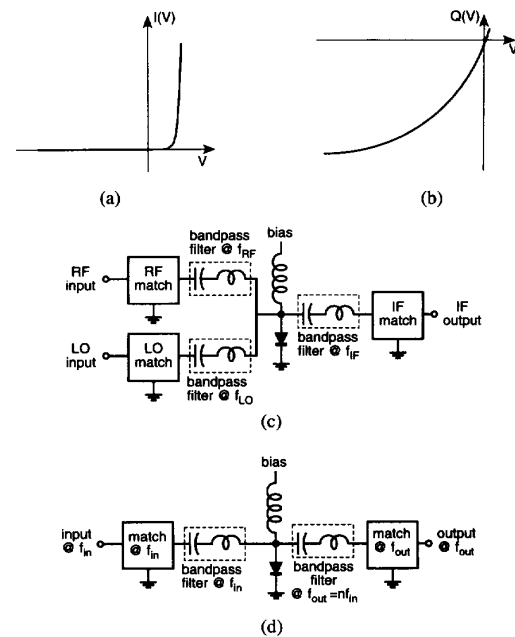

Fig. 3. The nonlinear current–voltage (a) and charge–voltage (b) characteristics of Schottky diodes are used in mixers (c) and frequency multipliers (d).

cannot generate pulses or measure broadband signals. This limitation drives us to distributed circuits.

III. DISTRIBUTED CIRCUITS AND DEVICES

In this section, we compare the bandwidths obtainable from lumped and distributed circuits. Linear distributed networks (circuits) permit a group of devices to be driven efficiently over a broad bandwidth. In contrast, impedance-matching networks are frequency-selective and allow efficient coupling to semiconductor devices only over narrow fractional bandwidths [38].

Distributed circuits, which incorporate a set of lumped semiconductor devices into a transmission line, obtain wider bandwidths than circuits incorporating a single lumped semiconductor device. Recognizing the advantages of distribution, we will also consider the case where the semiconductor device itself is distributed. We will find that fully distributed semiconductor devices have high microwave losses. Consequently, distribution is best applied at the circuit level.

A. Distribution and Gain–Bandwidth Limits

To examine the relative frequency limits of lumped and distributed circuits, consider three canonical amplifiers: a resistively terminated amplifier (Fig. 5(a)), a resonant impedance-matched amplifier (Fig. 5(b)), and a distributed amplifier (Fig. 7). Figure 4(a) shows a simplified HEMT small-signal model. Driven by a current source $I_{\mathrm{in}}(\omega)$, with the output grounded (Fig. 4(b)), the short-circuit current gain is

$$I_{\mathrm{out}}(\omega)/I_{\mathrm{in}}(\omega) = \omega_\tau/j\omega$$
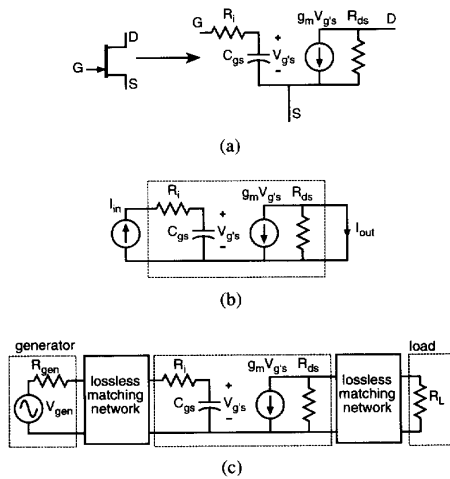
Fig. 4. The simplified circuit model of a high-electron-mobility transistor (HEMT) (a), and the definitions of short-circuit current gain (b), and maximum available power gain (c).
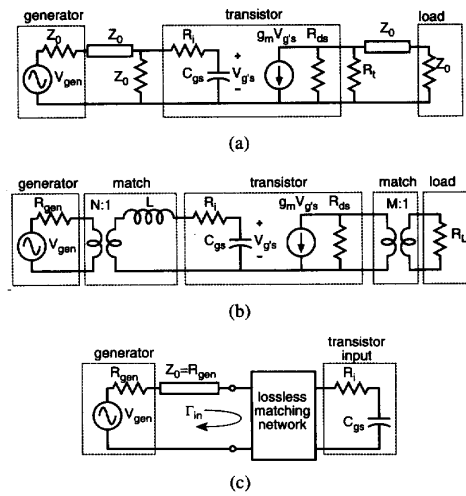

Fig. 5. Equivalent-circuit models of a resistively terminated amplifier (a) and a resonant impedance-matched amplifier (b). The transformer ratios are $N^2 = R_{gen}/R_i$ and $M^2 = R_{ds}/R_L$. Fano's inequality places an upper bound on the bandwidth over which the device can be impedance-matched (c).

where $\omega_\tau = g_m/C_{gs}$ is the current-gain cutoff frequency. If impedance-matched to both generator and load (Fig. 4(c)), the transistor provides its maximum available power gain

$$P_{\text{load}}/P_{\text{av,gen}} = G_{\max}(\omega) = (\omega_{\max}/\omega)^2$$

where

$$\omega_{\max} = \omega_\tau \sqrt{R_{ds}/4R_i}$$

is the power-gain cutoff frequency and

$$P_{\text{av},g} = V_{\text{gen}}^2/4R_{\text{gen}}$$

is the power available from the generator. The transistor parameters $C_{gs} = \tilde{C}_{gs}W_g$, $g_m = \tilde{g}_mW_g$, $R_i = \tilde{R}_i/W_g$, and $R_{ds} = \tilde{R}_{ds}/W_g$ scale with gate width (device size) W_g; $\omega_{\max}$ and ω_τ are independent of W_g.

The resistively terminated amplifier (Fig. 5(a)) is representative of most analog high-frequency amplifiers. Resistors at the input (Z_0) and output (R_t, chosen such that $R_t\|R_{ds} = Z_0$) terminate the transmission lines interfacing the amplifier to generator and load. The amplifier power gain is $\|S_{21}\|^2$, where $S_{21} = A_0/(1 + j\omega/\omega_p)$, the low-frequency gain is $A_0 = -g_mZ_0/2$, and the 3-dB bandwidth is

$$\omega_p = [C_{gs}(R_i + Z_0/2)]^{-1}.$$

In the limit $R_i = 0$, the amplifier gain–bandwidth product GBW $= |A_0|\omega_p = \omega_\tau$ is finite, yet the transistor power–gain cutoff frequency $\omega_{\max}$ is infinite. The resistively terminated amplifier does not use the transistor efficiently.

The impedance-matched amplifier (Fig. 5(b)), representative of most microwave amplifiers, uses transformers and a series inductor $L = 1/(\omega_0^2 C_{gs})$ which resonates with C_{gs} at the design frequency ω_0. At ω_0 the power gain is $G_{\max}$, but the circuit obtains this gain only over a narrow bandwidth; if R_i is small ($\omega_0R_iC_{gs} \ll 1$), the 3-dB bandwidth is

$\Delta\omega = 2\omega_0(\omega_0R_iC_{gs})$, a fraction of the center frequency ω_0. The amplifier uses the transistor efficiently only over a narrow bandwidth.

It is not possible to impedance-match over an arbitrarily wide bandwidth to a load with reactance. The power absorbed by the transistor input (Fig. 5(b)) is

$$P_{\text{in},t} = P_{\text{av},g}(1 - \|\Gamma_{\text{in}}\|^2)$$

and the power delivered to the load

$$P_{\text{load}} = G_{\max}P_{\text{in},t}$$

where Fano's limit [39] places an upper bound on the bandwidth over which the input reflection coefficient Γ_{in} is small (Fig. 5(c)) [38]

$$\int_0^{+\infty} \frac{1}{\omega^2} \ln\left(\frac{1}{\|\Gamma_{\text{in}}\|}\right) d\omega \leq \pi R_iC_{gs}. \tag{1}$$

In distributed circuits, device parasitic capacitances are absorbed into synthetic (periodic) transmission lines. A synthetic line (Fig. 6(a)) is a network of series impedances Z_s and shunt admittances Y_p. At frequency ω, waves propagate according to

$$V_{n+1} = V_n \exp\left(-\alpha(\omega) - j\beta(\omega)\right)$$

where

$$\cosh(\alpha + j\beta) = 1 + Z_sY_p/2.$$

The characteristic impedance is

$$Z_0 \equiv V_{\text{in}}/I_{\text{in}} = \sqrt{Z_s/Y_p}\sqrt{1 + Z_sY_p/4}.$$

An LC synthetic line (Fig. 6(b)) has zero attenuation ($\alpha = 0$) for frequencies below the Bragg periodic cutoff frequency
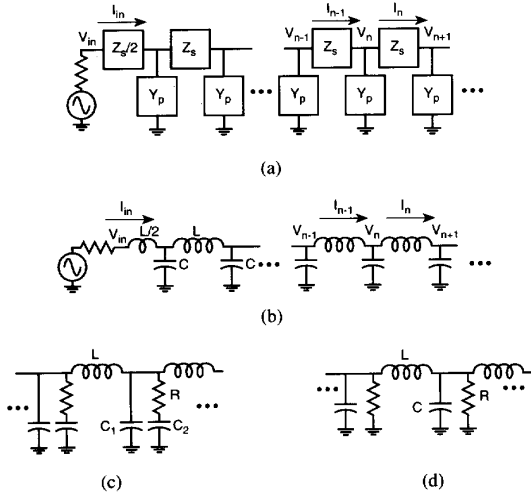
$$\omega_{\text{per}} = 2/\sqrt{LC}$$

Fig. 6. General synthetic (periodic) transmission line (a), ideal L–C synthetic line (b), and synthetic lines with frequency-dependent (c) and frequency-independent (d) dissipation.

Fig. 7. The HEMT distributed amplifier (a), and its small-signal model (b).

but very high attenuation for $\omega > \omega_{\mathrm{per}}$, has impedance

$$Z_0 = \sqrt{L/C}\sqrt{1 - \omega^2/\omega_{\mathrm{per}}^2}$$

and has per-section phase delay

$$
\begin{aligned}
T_d &\equiv \beta/\omega \\
&= (1/\omega)\arccos\left(1 - 2\omega^2/\omega_{\mathrm{per}}^2\right) \\
&= \sqrt{LC}(1 + \omega^2/6\omega_{\mathrm{per}}^2 + \cdots).
\end{aligned}
\tag{2}
$$

At frequencies well below ω_{per}, the LC synthetic line is a lossless transmission line with impedance $\sqrt{L/C}$ and per-section delay $\sqrt{LC}$. Adding a small series resistance R in series with a portion C_2 of the shunt capacitance (Fig. 6(c)), introduces frequency-dependent attenuation:

$$\alpha \cong \omega^2 C_2^2 R Z_0/2$$

for $\omega \ll \omega_{\mathrm{per}}$. Adding a large shunt loading resistance (Fig. 6(d)) also introduces attenuation $\alpha \cong Z_0/2R$.

The HEMT distributed or traveling-wave amplifier (TWA) is a broadband circuit whose gain–bandwidth product is limited by $\omega_{\max}$ (Fig. 7(a)) [40], [41]. The TWA exhibits the salient features of most distributed circuits. A synthetic transmission line (Fig. 7(b)) is formed in the gate circuit from the inductors L_g and the transistors' input impedances; for frequencies

$$\omega \ll \omega_{\mathrm{per},g} = 2/\sqrt{L_g C_{gs}}$$

the characteristic impedance is

$$Z_g \cong \sqrt{L_g/C_{gs}}$$

the per-section delay is

$$T_g \equiv \beta_g/\omega \cong \sqrt{L_g C_{gs}}$$

and the per-section attenuation is
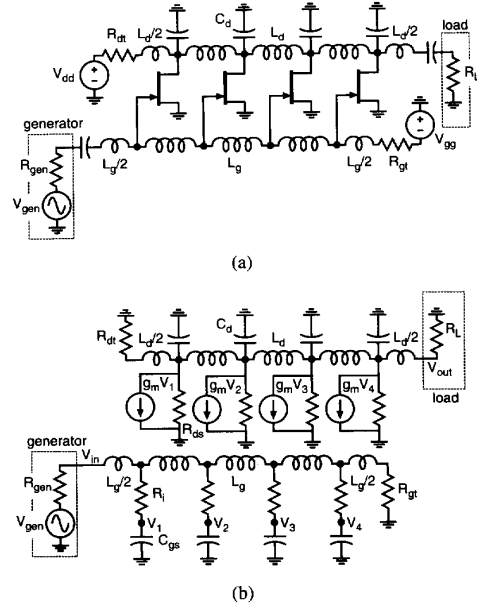
$$\alpha_g \cong \omega^2 C_{gs}^2 R_i Z_g/2.$$

A synthetic drain transmission line is formed from the inductors L_d and capacitors C_d; for frequencies

$$\omega \ll \omega_{\mathrm{per},d} = 2/\sqrt{L_d C_d}$$

the characteristic impedance is

$$Z_d \cong \sqrt{L_d/C_d}$$

the per-section delay is

$$T_d \equiv \beta_d/\omega \cong \sqrt{L_d C_d}$$

and the per-section attenuation is

$$\alpha_d \cong Z_d/2R_{ds}.$$

The lines are terminated by their characteristic impedances, $Z_g = R_{\mathrm{gen}} = R_{gt}$ and $Z_d = R_L = R_{dt}$.

For each transistor, the input signal propagates as a wave through a fraction of the gate line before driving that transistor's input and producing a drain current $g_m V_{gs}$. The drain current generates a forward wave on the drain line of amplitude $g_m V_{gs} Z_d/2$ which propagates to the amplifier output. Adding all transistor contributions for a TWA with N transistors, the gain is [42]

$$
\begin{aligned}
\frac{V_{\mathrm{out}}}{V_{\mathrm{in}}} \cong &\left(\frac{-g_m Z_d}{2}\right) \\
&\times \sum_{n=1}^{N} \exp\left(-\left(n - \frac{1}{2}\right)(\alpha_g + j\beta_g)\right. \\
&\left. -\left(N - n + \frac{1}{2}\right)(\alpha_d + j\beta_d)\right).
\end{aligned}
\tag{3}
$$

TWA gain–bandwidth is limited by gate-line and drain-line losses and by delay mismatch $\Delta T = T_g - T_d$.

Examining delay mismatch alone (setting $\alpha_g = \alpha_d = 0$), the gain is

$$\left\|\frac{V_{\text{out}}(\omega)}{V_{\text{in}}(\omega)}\right\| \cong \frac{g_m Z_d}{2}$$

$$\times \left\|\sum_{n=1}^{N} \exp\left(-j(n-1)\omega\Delta T\right)\right\|$$

$$\cong \frac{N g_m Z_d}{2}$$

$$\times \left(1 - \frac{(N\omega\Delta T)^2}{24}\right) \qquad (4)$$

where the second approximation is to leading order in N and $\omega\Delta T$. The gain decreases at high frequencies ($N\omega\Delta T \sim 1$) because the N transistor outputs do not add in phase. Bandwidth limits arising from delay mismatch (4) are eliminated by setting $T_g = T_d$.

Examining gate-line losses, the input voltage to the Nth transistor is attenuated by $e^{-(N-1/2)\alpha_g}$. Given a desired high-frequency cutoff ω_{high}, increasing the number of transistors beyond N_{max}, given by

$$N_{\text{max}}\omega_{\text{high}}^2 C_{\text{gs}}^2 R_i Z_g \simeq 1 \qquad (5)$$

does not increase the high-frequency gain because transistors far from the input are not driven. This is Ayasli's criterion [42].

Examining the drain-line losses, the output of the 1st transistor is attenuated by $e^{-(N-1/2)\alpha_d}$. Increasing the number of transistors beyond N_{max} given by

$$N_{\text{max}} Z_d / R_{ds} \simeq 1 \qquad (6)$$

does not increase the amplifier gain because transistors near the input do not contribute to the amplifier output.

Finally, the TWA gain drops rapidly for $\omega > \omega_{\text{per},g}$ or $\omega > \omega_{\text{per},d}$. These Bragg frequencies can be increased arbitrarily by using a large number of very small devices. Since

$$Z_g = \sqrt{L_g / C_{gs}}$$

and $T_g = T_d$, the gate and drain Bragg frequencies

$$\omega_{\text{per},d} = \omega_{\text{per},g} = 2 / W_g Z_g \tilde{C}_{gs}$$

vary inversely with the transistor gate width W_g. Since the amplifier voltage gain is

$$V_{\text{out}} / V_{\text{in}} \cong -N W_g \tilde{g}_m Z_d / 2$$

decreasing the transistor gate widths W_g while maintaining a constant total transistor gate width $N W_g$ increases the Bragg frequency while maintaining constant gain.

The TWA gain–bandwidth product is found from (5) and (6), where the low-frequency power gain is

$$G_{\text{power}} = (N g_m Z_d / 2)^2 Z_g / Z_d.$$

Combining these

$$G_{\text{power}}\omega_{\text{high}}^2 = \left(\frac{g_m}{2C_{gs}}\right)^2 \frac{R_{ds}}{R_i} = \omega_{\text{max}}^2. \qquad (7)$$
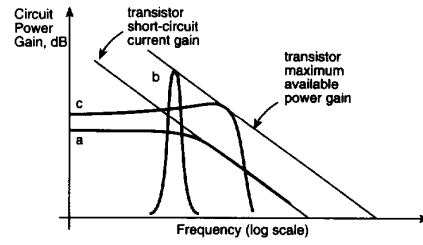

Fig. 8. Gain–frequency constraints of wideband lumped-element (a), resonant (b), and distributed (c) amplifiers .

The gain–bandwidth product is constrained by the transistor power-gain cutoff frequency. The TWA uses the transistors efficiently.

The three amplifiers discussed above illustrate the general properties of lumped and distributed circuits. A lumped, resistively terminated amplifier is nonresonant, but has its bandwidth limited by the device input capacitance C_{gs} and attains power gains well below those available from the device. Impedance matching allows the full power gain of a lumped device to be extracted over a narrow passband. In a distributed circuit, the lumped device is replaced by a large number of small devices distributed along a transmission line. The Bragg frequency can be increased arbitrarily by using a large number of very small devices. For strong coupling between two propagating waves in a distributed circuit or distributed device with per-section delay mismatch ΔT, the phase mismatch $\Delta\theta$ must be small at all frequencies of interest

$$\Delta\theta = N\omega\Delta T < \pi. \qquad (8)$$

The transmission line losses in the distributed circuit must also be small, e.g.

$$N\alpha(\omega) < 1/2 . \qquad (9)$$

Since the line losses α arise only from the resistive components of the device terminal impedances, performance is limited only by the fundamental energy-dissipating device parasitics, and not by capacitance charging times. Gain–frequency curves of the resonant, wideband lumped element, and distributed circuits are shown in Fig. 8. Other examples of linear distributed devices, with the same general properties, include traveling-wave photodetectors [43], microwave traveling-wave tubes [44], and traveling-wave electrooptic modulators [45].

B. Fully Distributed Semiconductor Devices

The TWA and the active and nonlinear wave propagation devices described later in this paper are distributed networks or circuits. It is natural to consider whether all such distributed circuits would instead be better constructed in a fully distributed form, e.g., with the distribution applied to the semiconductor devices themselves. TWA's incorporate a series of inductors (implemented using high-
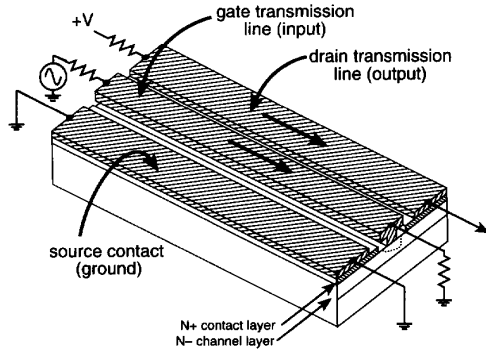
Fig. 9. A fully distributed traveling-wave transistor amplifier. Such a device would likely have high microwave losses.

Fig. 10. Wave height vrsus position of a surface wave, with a pulse profile, on water. The wave will reshape as it propagates.

impedance transmission lines) and lumped semiconductor devices (transistors) within an integrated circuit (Fig. 7); the TWA uses periodic distribution applied at the circuit level. A fully distributed HEMT TWA (Fig. 9) would be a single long transistor with the extended source, gate, and drain electrodes of the transistor itself used as transmission-line conductors carrying propagating waves. In this case, the semiconductor device itself is distributed. There are serious difficulties with fully distributed semiconductor devices.

One difficulty is semiconductor losses. Doped semiconductor layers are neither good dielectrics nor good conductors. Both the *transverse* fields and the *longitudinal* currents associated with transmission lines must be kept out of the conducting layers if high dielectric and conductor (semiconductor surface impedance) losses are to be avoided. This is difficult to accomplish if the transmission line and semiconductor device are merged into a common structure.

A second difficulty is the large disparity in the dimensions required for high-frequency semiconductor devices versus transmission lines. A HEMT with $f_{max} \sim 400$ GHz requires 2–3-μm separation between source and drain contacts and ~ 0.1-μm gate contact width. Wide transmission lines have high radiation loss [46], while narrow lines have high skin-effect loss [47]; loss is smallest when the line widths are roughly 1/10 of a wavelength in the dielectric. For use at 100 GHz, a CPW line on GaAs should be ~ 90 μm wide. If merged into a common, fully distributed structure, the transmission lines and semiconductor devices must share common dimensions, which must result in either poor device or transmission-line characteristics.

Finally, there is no clear motivation for a fully distributed TWA. If a periodically distributed TWA attains a gain–bandwidth product equal to the transistor ω_{max}, a fully distributed TWA using the same device cannot attain higher performance; the transistor cannot provide more than its maximum available gain.

Similarly, although a fully distributed nonlinear transmission line (NLTL, Section V) might be considered, a well-designed periodically distributed NLTL attains a rise time limited by the diode cutoff frequency, hence a fully distributed NLTL can perform no better. Worse, for reasons
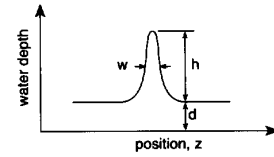
cited above, a fully distributed NLTL would have high microwave losses.

In distributed circuits, whether TWA's or nonlinear wave propagation devices, physical design of the transmission lines and of the semiconductor devices are independent, and high performance is obtained for both components. In a distributed circuit, the distribution must be periodic, and a Bragg frequency ω_{per} is therefore introduced. Using many small devices at small spacings, ω_{per} is increased to the point where bandwidth is limited by fundamental parameters of the semiconductor devices employed.

IV. NONLINEAR WAVE PROPAGATION

In the previous section, properties of linear distributed networks were explored. Introducing nonlinear semiconductor devices into a distributed network results in nonlinear wave propagation. Nonlinear wave propagation effects, specifically shock formation and signal decomposition into solitons, can be used for picosecond electrical pulse generation. As distributed networks, nonlinear wave propagation devices have the bandwidth necessary to support propagation of picosecond signals.

Similar nonlinear wave propagation effects frequently arise in nature. A familiar case, the propagation of surface waves on shallow water, will be used here to introduce the topic.

For small amplitudes, waves propagate on the surface of water as

$$h(z, t) = h_0 \cos(\omega t - \beta z)$$

where h is the vertical displacement of the water surface and

$$\omega^2 = \beta g \tanh(\beta d)$$
$$\simeq \beta^2 g d - \frac{1}{2}\beta^4 g d^3 - \cdots. \tag{10}$$

$g = 9.81$ m/s^2 is the gravitational acceleration and d is the water depth. The phase velocity is $v_p = \omega/\beta$.

A small-amplitude pulse of full-width at half-maximum length w (Fig. 10) has a Fourier spectrum with wavelengths $\lambda = 2\pi/\beta$ extending from $\lambda \simeq w$ to infinity. If the pulse length is long ($w \gg d$), all Fourier components will have $\beta d \ll 1$ and will propagate at velocity $\sqrt{gd}$; the wave shape will not change during propagation (Fig. 11(a)). This is linear, nondispersive propagation.

If the pulse length is short ($w \sim d$), some Fourier components will have wavelengths comparable to the water depth ($\beta d \sim 1$), and will propagate more slowly than longer
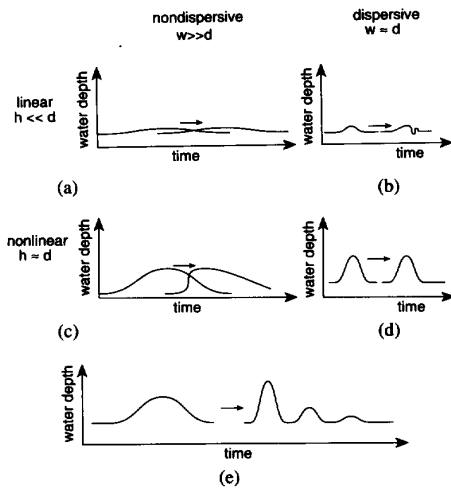
Fig. 11. Propagation of surface waves on water: linear nondispersive propagation (a), linear dispersive propagation (b), nonlinear nondispersive propagation and shock formation (c), nonlinear dispersive propagation and soliton propagation (d), and soliton decomposition (e).

wavelengths (10). The wave is reshaped during propagation (Fig. 11(b)). This is linear, dispersive propagation.

If the amplitude is comparable to the depth ($h \sim d$), nonlinear propagation results. If the pulse length is also much larger than the depth, dispersion is avoided ($\beta d \ll 1$) and (10) the velocity varies as the square root of the depth,

$$v_p = \sqrt{g(d + h(z,t))}.$$

The water depth is modulated significantly by the wave amplitude itself, and different portions of the wave propagate at different velocities. The leading edge of a positive-going wave will steepen during propagation (Fig. 11(c)) until the wavefront becomes nearly vertical (e.g., a shock wave is formed), whereupon the wave energy will be dissipated by water spilling over the leading edge. This is the familiar wave-breaking effect observed at the beach or in tidal bores. Shock waves result from the competition between nonlinearity (amplitude-dependent wave velocity) and dissipation, with negligible dispersion. Shock waves are observed on water, in acoustics (explosions), and in ionized gases [48]–[50].

If the amplitude is comparable to the depth and the pulse length is short ($w \sim d$), then both dispersion and nonlinear propagation are significant. In general, a pulse will be reshaped during propagation. For certain specific wave shapes, the effects of dispersion and nonlinearity counteract each other, and the wave will propagate without distortion (Fig. 11(d)). These are called solitary waves. *Solitons* are those solitary waves which also preserve their amplitude and shape after collision with other solitons [14]. The nonlinear, dispersive propagation of surface waves on water is described to leading order by the Korteweg–deVries (KdV) equation [51], which predicts soliton propagation. For the KdV equation, if a wave is launched whose shape is not that of a soliton, the wave will decompose during

propagation into a set of solitons having differing propagation velocities (Fig. 11(e)), which will therefore progressively separate during propagation [52]. Solitons result from the competition between nonlinearity (amplitude-dependent wave velocity) and dispersion, with negligible dissipation. Solitons are observed on water, in ionized gases, and in optical fibers [48], [50], [53].

Nonlinear wave propagation is used extensively in optics. In optical fibers the refractive index $n = n_0 + kE^2$ and the velocity of propagation c/n are modulated in proportion to the square of the electric field E. Fiber-grating pulse compressors use this index nonlinearity in combination with the dispersion of an external diffraction grating pair to compress optical pulses to durations as short as 6 fs [10]. The fibers themselves exhibit dispersion, and with sufficient intensities will propagate solitons. Optical soliton propagation has been used for dispersionless signal propagation in fiber-optic transmission, and for optical switching [53]. Solitons on optical fibers are governed by the nonlinear Schrödinger equation, and differ considerably from solitons on water or on NLTL's. Optical solitons are *envelope* solitons (a sinusoidal optical carrier intensity-modulated by a pulse envelope), and the velocity varies only to second order in the wave amplitude.

V. The Shock-Wave NLTL

Both shock-wave formation and soliton propagation on nonlinear transmission lines (NLTL's) are used for electrical pulse generation. The NLTL, a distributed nonlinear capacitance, is the distributed counterpart of the silicon step-recovery diode (SRD), a lumped-element nonlinear capacitor used for pulse and microwave harmonic generation [54]. SRD's are widely used to strobe diode sampling bridges [55] used in microwave network analyzers, sampling oscilloscopes, and frequency synthesizers. The $\sim$35-ps pulse rise times attainable with silicon SRD's have limited sampling circuit, hence instrument bandwidths to $\sim$ 30–50 GHz. Shock-wave NLTL's can generate subpicosecond step functions, extending sampling circuit and instrument bandwidths to beyond 700 GHz. Several commercial high-performance microwave instruments using NLTL-gated sampling circuits have recently been introduced [56], [57].

The GaAs NLTL [12], [13], [15], [16], [18] (Fig. 12(a)) is a monolithic circuit consisting of a high-impedance line of impedance Z_1 loaded at spacings d (spacings of $\tau = d/v_{\rm cpw}$ in units of time delay) by reverse-biased Schottky diodes serving as voltage-variable capacitors. $v_{\rm CPW}$ is the propagation velocity of the high-impedance coplanar waveguide (CPW) line sections. Figure 12(b) shows the equivalent circuit, where

$$L = Z_1\tau \text{ and } C_l = \tau/Z_1 \tag{11}$$

are the line section inductance and capacitance, and $C_d(V)$ and R_d are the diode capacitance and parasitic series resistance. The diode cutoff frequency is $\omega_d = 1/C_d(V)R_d$ at bias voltage V.
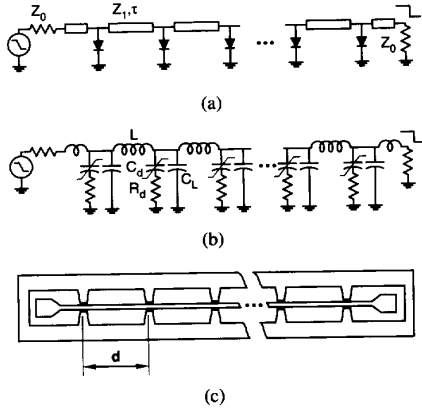
Fig. 12. Circuit diagram (a), equivalent circuit (b), and layout (c), of a nonlinear transmission line.

Fig. 13. NLTL wavefront compression with step-function input (a). Propagation and evolution of a partial shock wavefront (b).

The NLTL is a synthetic transmission line having a periodic-line (Bragg) cutoff frequency

$$\omega_{\mathrm{per}} = 2/\sqrt{L(C_l + C_d(V))}$$

strong group-delay dispersion arises for $\omega \simeq \omega_{\mathrm{per}}$ (2). The variable diode capacitance introduces a desired reduction in propagation delay with increasing reverse bias, resulting in the reduction of the fall time of waves propagating on the NLTL.

Consider an idealized NLTL where $R_d = 0$ and ω_{per} is made very large by reducing both the diode spacings d and the diode capacitances $C_d(V)$, such that the diode capacitance per unit length $C_d(V)/d$ remains constant. In this limit of a continuous line [13], the voltage at the nth diode is

$$V_n(t) = V_{\mathrm{in}}(t - nT(V)) \tag{12}$$

where

$$T(V) = \sqrt{LC_T(V)} \tag{13}$$

is the propagation delay and $C_T(V) = C_l + C_d(V)$ is the total capacitance per NLTL section. The variation in propagation delay $T(V)$ results in the compression of negative-going wavefronts during propagation. As an input signal $V_{\mathrm{in}}(t)$, a falling step function with initial voltage V_h, final voltage V_l, and (input) fall time $T_{f,\mathrm{in}}$, propagates on the line, the fall time $T_{f,n}$ at the nth NLTL section will at first decrease linearly with distance (Fig. 13(a))

$$T_{f,n} = T_{f,\mathrm{in}} - n\Delta T$$
$$= T_{f,\mathrm{in}} - n(T(V_h) - T(V_l)). \tag{14}$$

After a sufficient number of NLTL sections, (12) and (14) predict that the fall time will become less than zero. At this point, the voltage $V_n(t)$ becomes discontinuous, forming a shock wave, and (12), and (14) apply only to the continuous portions of $V_n(t)$ outside of the shock wavefront. The number of NLTL sections necessary to form a shock wave
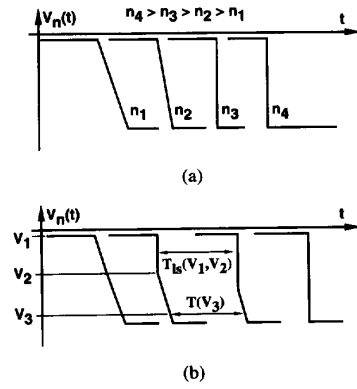
is $n \simeq T_{f,\mathrm{in}}/\Delta T$. Shock formation on NLTL's is similar to the breaking of surface waves on water (Section IV).

Shock waves have propagation properties determined by the large-signal diode capacitance C_{ls}

$$C_{ls}(V_l, V_h) = \frac{1}{V_h - V_l} \int_{V_l}^{V_h} C_d(V)\, dV. \tag{15}$$

After formation, the shock wave has a per-section propagation delay of [13]

$$T_{ls}(V_l, V_h) = \sqrt{L(C_l + C_{ls}(V_l, V_h))}. \tag{16}$$

In general, the shock wave first forms as a partial-amplitude shock wave (Fig. 13(b)). The partial shock between V_1 and V_2 has a per-section propagation delay of $T_{ls}(V_1, V_2)$, while the more negative voltages in the vicinity of V_3 have a smaller propagation delay $T(V_3)$, and the point of the waveform at voltage V_3 thus eventually joins the shock wavefront. The partial shock amplitude grows with propagation, and a shock wave of full amplitude is eventually formed. For step-functions propagating on the NLTL after shock formation, the voltage V_n and current I_n are related by a constant large-signal wave impedance

$$Z_{ls}(V_l, V_h) = \sqrt{\frac{L}{C_l + C_{ls}(V_l, V_h)}}. \tag{17}$$

Shock waves are propagated without reflection or distortion from the NLTL to the load if $Z_{ls}(V_l, V_h) = Z_{\mathrm{load}}$.

With nonzero ω_d and ω_{per} the shock fall time will asymptotically approach a minimum compressed fall time $T_{f,\mathrm{min}}$ at which wavefront compression ΔT is balanced by the wavefront spreading associated with ω_d and ω_{per}.

If the diode cutoff frequency dominates ($\omega_d < 5\omega_{\mathrm{per}}$), shock formation competes with high-frequency dissipation in the diode series resistance. For a uniformly doped Schottky diode, the diode capacitance is given by

$$C_d(V) = C_{j0}/\sqrt{1 - V/\phi}$$

and

$$T_{f,\mathrm{min}(10\%-90\%)} = \frac{8.8}{\omega_d(0)} \frac{1}{\sqrt{1 - V_l/\phi} - 1} \tag{18}$$
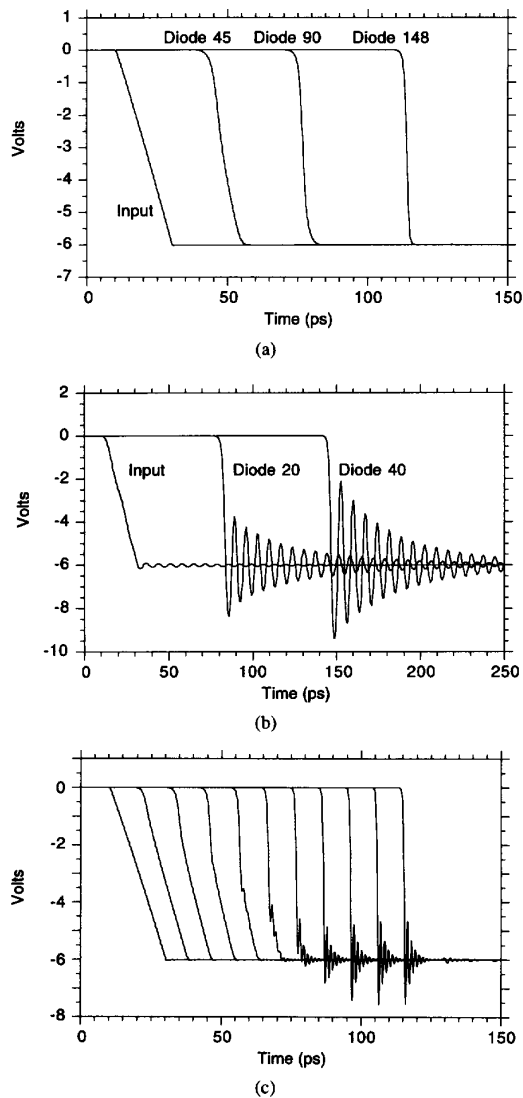
Fig. 14. SPICE simulations of fall-time compression showing the relative effects of the diode and Bragg frequencies. 2.9-ps fall-time NLTL shock formation with diode cutoff frequency dominant (500-GHz diode and Bragg frequencies) (a). 2.4-ps fall-time NLTL shock formation with Bragg frequency dominant; (100-GHz Bragg frequency, 2-THz diode cutoff frequency) (b). 0.9-ps fall-time NLTL shock formation with Bragg and diode cutoff frequencies chosen to have comparable effects on compressed fall time (500-GHz Bragg frequency, 2-THz diode cutoff frequency) (c). Partial shock formation is also evident. Voltages are shown at 15-diode intervals.

assuming that $V_h = 0$ volts [9]. For more general diode doping profiles, circuit simulations are used to predict $T_{f,\min}$. A large-signal cutoff frequency $\omega_{d,ls} = 1/R_s C_{ls}$ is defined, with $T_{f,\min} \propto 1/\omega_{d,ls}$. Figure 14(a) shows a simulation of shock formation on a 150-section NLTL with the diode cutoff frequency dominant.

If the Bragg frequency dominates ($\omega_d \gg \omega_{\mathrm{per}}$) then $T_{f,\min} \propto 1/\omega_{\mathrm{per}}$, dispersion is the dominant high-frequency effect, and shock wavefronts show strong ringing
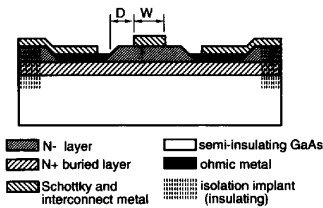
Fig. 15. Cross section of a Schottky varactor diode. The Schottky contact width is W and the separation between Schottky and ohmic contacts is D. The diode stripe length is L in the direction perpendicular to the plane of the figure.

at the Bragg frequency (Fig. 14(b)). If $\omega_d \gg \omega_{\mathrm{per}}$, shocks are formed only with step-function inputs; with either impulsive or sinusoidal inputs, trains of solitons are generated [15], [14].

ω_{per} and $\omega_{d,ls}$ have comparable effects on $T_{f,\min}$ if the diode cutoff frequency is 4–6 times the Bragg frequency. With ω_{per} and $\omega_{d,ls}$ in these proportions, shock waves are generated with moderate ringing (Fig. 14(c)).

VI. NLTL DESIGN

To function properly, the NLTL must have high Bragg and diode cutoff frequencies, sufficient diode breakdown voltage, low layout parasitics, low skin-effect losses, and strongly varying diode capacitance.

A cross section of the Schottky diode is shown in Fig. 15. To fabricate the diodes, an n^+ buried contact layer and an n^- diode active layer are grown on a semi-insulating GaAs substrate. Ohmic contacts are formed to the n^+ layer, and device areas are defined by a proton isolation implant which converts implanted semiconductor into insulator. Schottky contacts result where a deposited Ti/Pt/Au metal layer overlays the unimplanted n^- layer. Additional process steps are used to deposit transmission-line metallization and air-bridge interconnections.

The diode parasitics must now be considered. For the diode of Fig. 15, if uniformly doped, the depletion depth is

$$x_j = \sqrt{2\epsilon(\phi - V)/qN_d^-}$$

where ϵ is the dielectric constant and N_d^- the active layer doping, and the capacitance is $C_d(V) = \epsilon WL/x_j$. The series resistance can be modeled with three components. Series resistance includes ohmic-contact resistance $R_c = \rho_c/2L$, where ρ_c is the specific contact resistivity. The series resistance of the n^+ layer, including spreading resistance under the Schottky contact, is

$$R_{N+} = (\rho^+/T^+)[(D/2L) + (W/12L)]$$

where ρ^+ and T^+ are the resistivity and thickness of the n^+ layer. T^+ is limited by the maximum proton implant depth available, while ρ^+ is constrained by doping limits in growth. The portion of the n^- layer between the bottom of the depletion layer and the n^- to n^+ interface contributes a resistance at zero bias of $R_{N-} = (T^- - x_{j0})\rho_-/WL$ where ρ_- is the n^- resistivity and x_{j0} is the zero-bias depletion depth. R_{N-} is minimized by setting T^- equal to
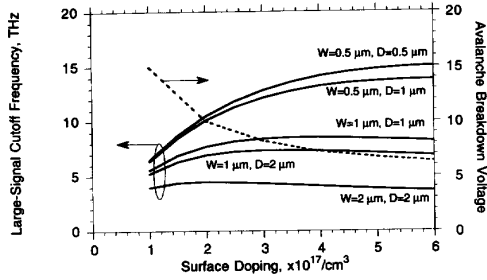
Fig. 16. Large-signal cutoff frequency and avalanche breakdown voltage versus surface doping and diode dimensions for uniformly doped Schottky diodes.

the depletion depth at the maximum anticipated reverse-bias voltage.

From these resistances and capacitances, the diode cutoff frequency can be determined. Figure 16 shows calculated diode cutoff frequencies using the process parameters $T^{+} +$ $T^{-} = 1.4 \ \mu m$, $\rho_c = 20 \ \Omega \cdot \mu m$, and $\rho^{+} = 7.5 \ \Omega \cdot \mu m$. The n^{-} layer thickness T^{-} is selected so that the layer is fully depleted at 7-V reverse bias. At 8–10-V reverse breakdown, 5–10-THz cutoff frequencies are attainable. Increasing the diode doping while decreasing the diode dimensions D and W increases the diode cutoff frequency. The diode cutoff frequency cannot be increased without bound because increasing the diode doping also decreases the diode reverse breakdown voltage. Given application of the NLTL as a strobe pulse generator for sampling circuits, the required diode reverse breakdown voltage is determined by the minimum NLTL voltage required to drive the sampling bridge (3–4 V) and by skin-effect losses. Because current NLTL's have ~2:1 attenuation, NLTL input voltages, and hence required breakdown voltages, are 8–10 V. The hyperabrupt diode doping profiles used in some NLTL's increase the fractional variation in capacitance, thereby increasing the NLTL compression per unit distance and decreasing the required length and the incurred skin-effect losses. As a penalty, with fixed process dimensions (D and W) and fixed breakdown voltage, hyperabrupt diodes have smaller cutoff frequencies than uniform diodes.

Physical design of the NLTL cell strongly influences performance. CPW skin loss must be minimized; the NLTL should be as short as possible, and hence must exhibit a large change in delay ΔT per unit distance. NLTL's cells either incorporate the diodes in the CPW ground plane (Fig. 17(a)) or underneath the NLTL center conductor (Fig. 17(b)). The dimensional ratio a/b is set by the CPW characteristic impedance, which on GaAs is

$$Z_1 \cong 11.3 \ \Omega \cdot \ln \left(2 \frac{1 + \sqrt[4]{1 - k^2}}{1 - \sqrt[4]{1 - k^2}} \right) \qquad (19)$$

for $0 \le k \le 1/\sqrt{2}$, where $k = a/(a + 2b)$. If the NLTL is to exhibit a large change in delay with voltage, the diode capacitance must both show a large variation with voltage and must dominate (14) over the transmission line
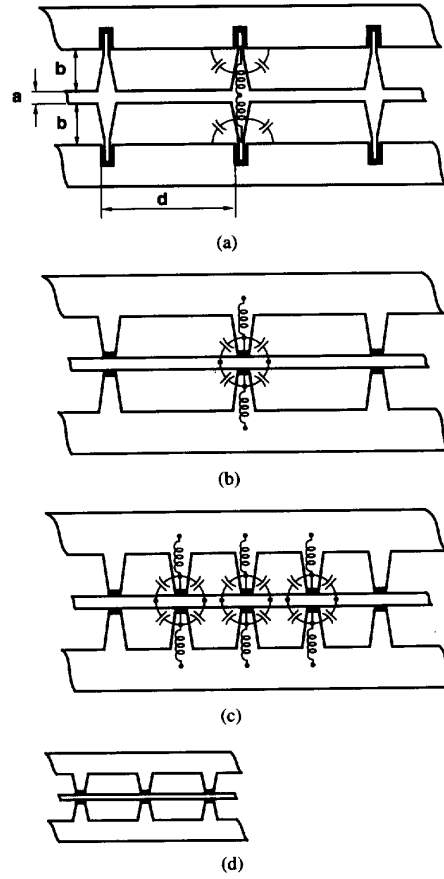

Fig. 17. Two alternative NLTL cells showing interconnection parasitics, (a) and (b). Parasitics will dominate if the CPW dimensions a and b are held constant when the Bragg frequency is scaled (c). To proportionally reduce parasitics while scaling the Bragg frequency, the CPW dimensions must also be scaled (d).

capacitance τ/Z_1. This requires (17) that Z_1 be at least 75 Ω for a $Z_{ls} = 50 \ \Omega$ NLTL, and a/b must therefore be small.

In either NLTL cell design the conductors interconnecting the diode and transmission line introduce parasitic layout inductance and capacitance, both of which become comparable to the CPW inductance L and capacitance C_l if d is equal to b (Fig. 17(c)). The CPW ground–ground spacing is therefore constrained to $1.5(a + 2b) \le d$. Small $T_{f, min}$ requires high ω_{per} and hence small d. The CPW ground–signal separation b then becomes small, as does (with fixed Z_1, (19)) the center conductor width a. The skin attenuation is

$$\alpha_{skin} = (nd/a)\sqrt{\omega\mu/2\sigma} \times (1/2Z_{LS})$$

where the required number of NLTL sections is $n \simeq T_{f, in}/\Delta T$. μ is the permeability of vacuum and σ the metal conductivity. The high Bragg frequencies required for small $T_{f, min}$ force narrow CPW dimensions and high CPW losses. The losses decrease the output amplitude, and increase output fall time because the reduced signal swing reduces the fractional variation in diode capacitance.
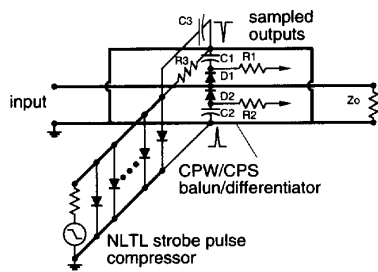
Fig. 18. Sampling circuit schematic diagram.

Fig. 19. Sampling circuit layout. Hold and matching capacitors $C1$–$C3$ are implemented using reverse-biased diodes.

The wavefront fall time decreases with distance (Fig. 14), hence high ω_{per} is only required near the NLTL output, where the transition times are short. To minimize losses, low-loss NLTL cells with low ω_{per} are used near the input, and higher loss (high ω_{per}) cells with small $T_{f,min}$ are used near the line output. The line is exponentially tapered, with the Bragg frequency at the nth NLTL section being given by $\omega_{per,n} = k\omega_{per,n-1}$ ($k > 1$).

VII. MILLIMETER-WAVE SAMPLING CIRCUITS

Sampling circuits [55], as used for signal measurement or frequency down-conversion in microwave instruments, are the primary application for the NLTL [9], [58].

A sampling circuit consists of a strobe pulse generator, a diode/resistor bridge, and a balun/differentiator. The circuit diagram is shown in Fig. 18 and its layout in Fig. 19. Capacitors $C1$–$C3$ are implemented as reverse-biased diodes. In the circuit an NLTL compresses an input strobe signal, either a step function or a microwave sine wave (10%–90% fall time $0.3/f_{input}$). The sampling diodes are gated by a pair of symmetric positive and negative impulses generated from the NLTL output using a balun/differentiator implemented using the coplanar strip (CPS) mode of the input signal coplanar waveguide (CPW). Coupled through the matching network R_3 and C_3, the strobe step function is applied between the CPW ground planes, and propagates on them in both directions as a CPS mode. At a distance d_{short} from the sampling diodes, short circuits between the two CPW ground planes reflect the CPS mode, generating balanced impulses at the sampling diodes of duration $2d_{short}/v_{CPW}$.

The complementary strobe pulses, coupled through hold capacitors C_1 and C_2, drive the sampling diodes into forward conduction. During this period, the sampling aperture time, the input (RF) signal partially charges C_1 and C_2. If the RF frequency is a multiple nf_0 of the strobe frequency (LO), at each successive strobe pulse the sampling diodes further charge C_1 and C_2, and the sampled outputs asymptotically charge to the RF input voltage. The sampled (IF) voltages developed at the two hold capacitors are fed through isolation resistors ($R1$ and $R2$) and applied to the high-impedance inputs of an operational-amplifier summing circuit. The RF frequency is offset by Δf from a multiple nf_0 of the strobe frequency f_0 and the sampled signal is then mapped out at a repetition frequency Δf (Fig. 20). The bridge is self-biased, with the diode conduction currents
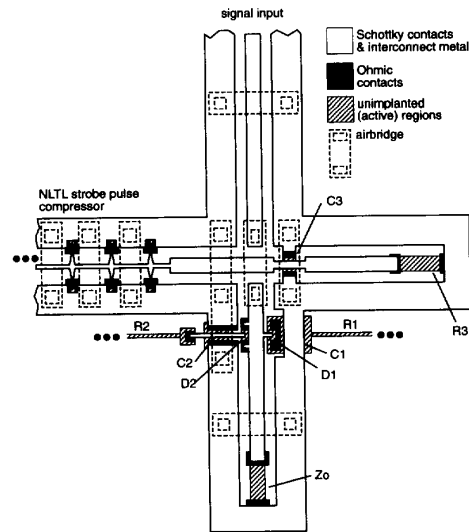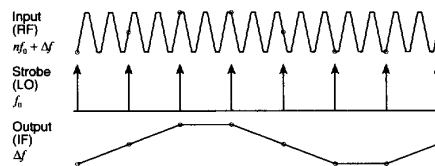

Fig. 20. Signal sampling. An input signal with repetition frequency $nf_0 + \Delta f$ sampled at repetition frequency f_0 produces an output at frequency Δf.

establishing charges on C_1 and C_2 which hold the diodes in reverse bias between strobe pulses.

The sampling circuit rise time is determined by the sampling diode capacitance charging time and by the aperture time. The sampling diode capacitances introduce a 10%–90% rise time of $2.2(Z_0/2)2C_{diode}$, where $Z_0 = 50\,\Omega$ and C_{diode} is the sampling diode capacitance. Aperture time is determined by the strobe fall time, by the differentiators' round-trip delay $2d_{short}/v_{CPW}$, and by the sampling diode reverse bias. With self-bias, the sampling diode bias is close to the strobe impulse peak amplitude, and the diodes conduct only for a fraction of the duration of the strobe pulse.

To evaluate the NLTL and sampling circuit rise time, the output of an NLTL shock generator is connected to an on-wafer NLTL-gated sampling circuit, thus yielding a measurement of their convolved responses. Figure 21 shows measured waveforms. With NLTL's and sampling circuits processed at 3-μm minimum device dimensions on hyperabrupt-doped material, the diode cutoff frequency is 1.7 THz and a 1.8-ps 10%–90% fall time is measured [9]. Under the assumption of equal fall times for the NLTL and sampling circuit, a 1.27-ps fall time and a 275-GHz bandwidth are determined for each component. With NLTL's and sampling circuits processed at 1-μm minimum
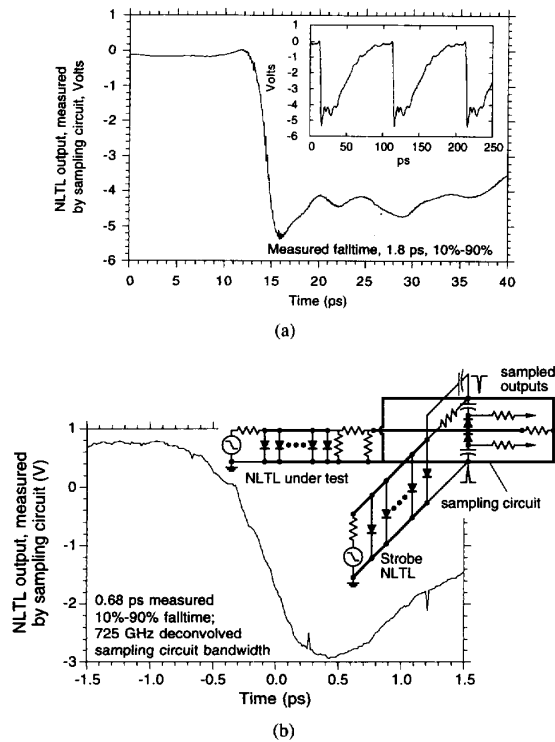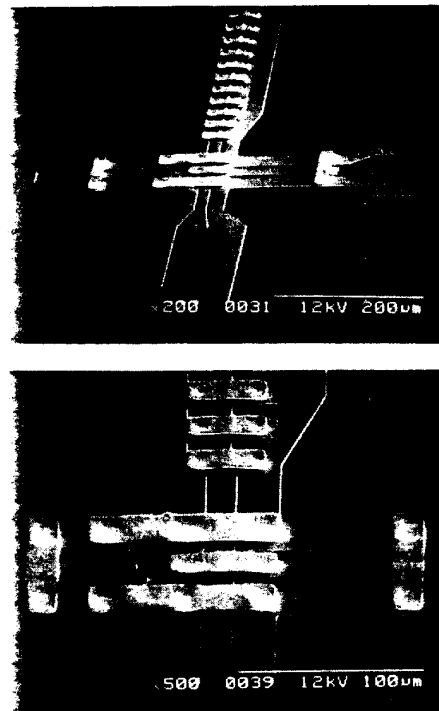
Fig. 21. NLTL and sampling circuit results; NLTL output waveforms as measured by on-wafer sampling circuits, using hyper-abrupt-doped material at 3-μm design rules (a) and uniform-doped material at 1-μm design rules (b).

Fig. 22. Scanning electron micrographs of a 515-GHz-bandwidth NLTL-gated sampling circuit.

device dimensions on uniform-doped material, the diode cutoff frequency is 4.1 THz and a 0.68-ps 10%–90% fall time is measured, with deconvolution yielding a 725-GHz sampling circuit bandwidth. A scanning electron micrograph of a 515-GHz samping circuit [59] is shown in Fig. 22. Other NLTL-gated sampling circuits have been reported by Marsland [58], [60], Yu [61], Shakouri [22], and Whitely [57].

NLTL and sampling circuit bandwidths can be further improved. Reducing transmission-line skin-effect losses will decrease the required NLTL input voltage and hence the required diode breakdown voltage. More heavily doped diodes with higher cutoff frequencies can then be used, reducing the compressed fall times $T_{f,min}$. Diode junction areas of 1 μm^2, or less, are required in both the sampling circuit and the NLTL to increase the Bragg frequency and to decrease the sampling diode capacitance charging time. NLTL transition times below 0.3 ps and sampling circuit bandwidths above 1 THz should be feasible.

VIII. SOLITON PROPAGATION DEVICES

Picosecond duration, large-amplitude electrical impulses can be generated through soliton propagation on NLTL's. Soliton propagation is also used for harmonic generation. Impulse compression through soliton propagation results in significant pulse amplitude increase in the absence of

skin-effect losses. If $\omega_d \gg \omega_{per}$, then diode dissipation is negligible and propagation is dominated by the interaction between the capacitive nonlinearity and the periodic-network dispersion, and soliton propagation results [15], [14], as discussed in Section IV.

A. Solitons on NLTL's

NLTL's provide a nonlinear, dispersive medium for soliton propagation [15], [18], [62]–[64]. If the nth diode (Fig. 12(a)) has capacitance $C_{n,d}(V)$ and the nth line section has impedance Z_1 and delay τ_n, then the NLTL is a synthetic transmission line with inductance $L_n = Z_1 \tau_n$, and total capacitance

$$C_n(V) = C_{n,d}(V) + \tau_n/Z_1$$

for the nth NLTL section. The NLTL has nonlinearity arising from the diodes, and dispersion arising from its periodicity (2). As with surface wave propagation on water, soliton propagation on NLTL's is described to leading order by the KdV equation.

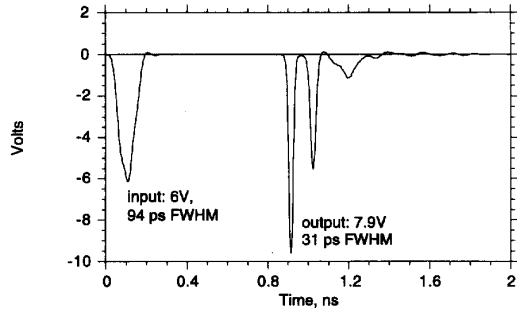If the capacitance at node n is approximated in the form

$$C_n(V) = C_0/(1 + V/V_0)$$

and $L_n = L$ for all n (i.e., if the line is homogeneous), the NLTL supports propagation of solitons [15] of the form

$$V_n(t) = V_{max} \operatorname{sech}^2(1.767(t - nT_d)/T_{fwhm}) \qquad (20)$$
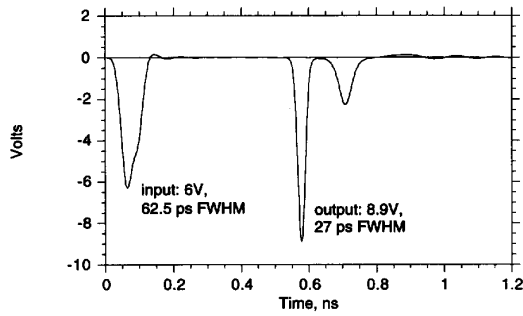
(a)

(b)

Fig. 23. Simulations of a narrow pulse decomposing into two solitons (a) and a wide pulse decomposing into three solitons (b) on a homogeneous line.

Fig. 24. Measured NLTL output waveform illustrating the decomposition of an input sine wave into two solitons per cycle.

Fig. 25. Simulated and measured conversion efficiency for an NLTL distributed frequency multiplier. In the absence of transmission-line skin-effect losses, relatively high efficiencies can be obtained over a broad bandwidth.

where

$$T_d = \sqrt{LC_0 V_0/V_{max}}\ \sinh^{-1}\left(\sqrt{\frac{V_{max}}{V_0}}\right) \qquad (21)$$

and

$$T_{fwhm} = 1.767 \sqrt{LC_0 V_0/V_{max}}. \qquad (22)$$

On the NLTL, impulses having duration

$$T_{fwhm} > 1.767 \sqrt{LC_0 V_0/V_{max}}$$

correspond to a nonlinear superposition of a set of solitons having differing amplitudes and hence differing per-section propagation delays T_d; applied to the NLTL, the impulse will decompose into this set of two or more solitons during propagation. Figure 23 shows circuit simulations of a narrow pulse decomposing into two solitons (Fig. 23(a)) and a wider pulse decomposing into three solitons (Fig. 23(b)) on a homogeneous NLTL.

B. Harmonic Generation

The splitting of input pulses into pairs of solitons is used as a method of second- and third-harmonic generation. Each negative-going lobe of an input sine wave separates during propagation into a set of solitons, generating a waveform with multiple pulses per cycle and significant harmonic content. Figure 24 shows measured output waveforms of an NLTL driven at a frequency slightly below $\omega_{per}/2$. Two solitons per signal cycle are observed and the signal has

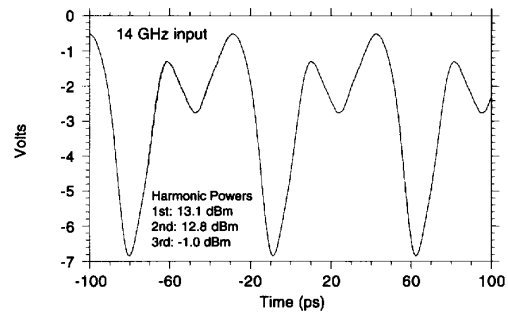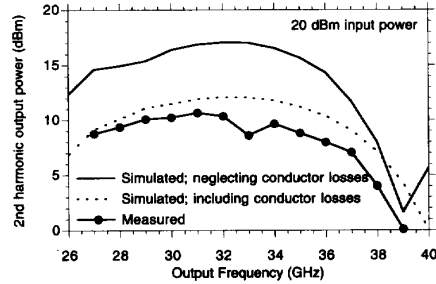a strong second-harmonic content. Conversion to second harmonic is most efficient if $\omega_{per}/3 < \omega_{input} < \omega_{per}/2$.

In Fig. 24, second-harmonic generation results from nonlinear wave propagation on an NLTL, a distributed nonlinear capacitance. Most millimeter-wave diode frequency multipliers consist of a lumped nonlinear element with associated filtering and impedance-matching networks (Fig. 3(d)). If the diode is used (Fig. 3(b)) as a nonlinear capacitor, then it must have significant capacitance, and Fano's inequality (Section III-A) then limits the bandwidth of the matching networks, limiting the bandwidth over which efficient second-harmonic generation can be obtained. The limited efficiency–bandwidth product of a lumped-element frequency multiplier and the limited gain–bandwidth product of lumped HEMT amplifier (Section III-A) arise from similar circuit design constraints.

An NLTL distributed frequency multiplier is a broadband distributed network. On NLTL's, relatively high second-harmonic-generation efficiencies can be obtained over broad bandwidths (Fig. 25), *if skin-effect losses are negligible* [65]. Skin-effect losses on current NLTL distributed frequency multipliers reduce the conversion efficiencies to levels comparable to lumped-element varactor frequency multipliers implemented in waveguide. Skin-effect losses can be substantially reduced by using elevated coplanar waveguide [22], in which airbridge fabrication processes are used to elevate the CPW signal conductor 1–3 μm above the substrate.
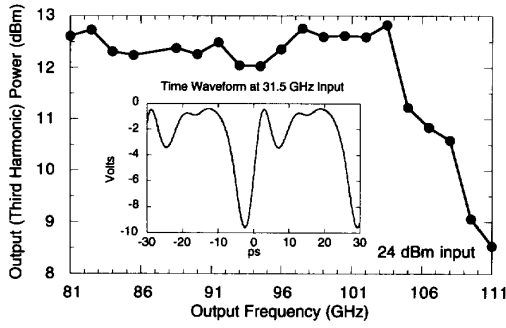
Fig. 26. Measured output power versus output frequency for an NLTL-distributed frequency tripler with $\omega_{per}/2\pi = 99$ GHz and 24-dBm input power. In the inset the output time waveform is shown at 31.5-GHz input.
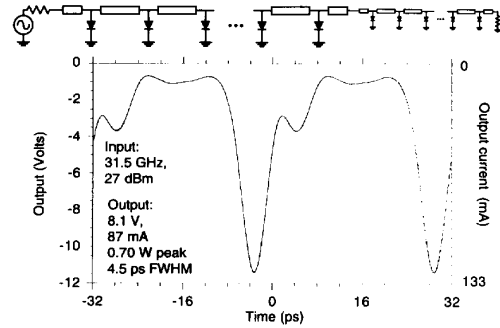
Fig. 27. Measured output waveform of a two-stage step-tapered soliton impulse compressor.

Fig. 28. Measured output waveform for a continuously tapered NLTL impulse compressor driven by a 26.6-dBm, 9-GHz sine wave.

Figure 26 shows the measured output waveform and measured conversion efficiency for a distributed frequency tripler [19]. Distributed frequency multipliers have also been reported by Marsland [66], and analyses reported by Champlin [67] and Scott [18].

C. Impulse Generation

A pulse with

$$T_{fwhm} > 1.767 \sqrt{LC_0V_0/V_{max}}$$

input to an NLTL will decompose into its characteristic set of solitons. Longer input pulses decompose into progressively larger numbers of solitons, and impulse compression ratios are limited to $\sim 2{:}1$ on a homogeneous line (Fig. 23).

Higher compression ratios can be obtained by using step-tapered lines, consisting of a line with Bragg frequency $\omega_{per,1}$ cascaded with a line with Bragg frequency $\omega_{per,2} = 2\omega_{per,1}$. The first line section performs a 2:1 pulse compression, with the second line section performing a further 2:1 compression (Fig. 27), for a net $\sim 4{:}1$ compression. While higher compression ratios can be obtained by repeating this scheme in a three-step or four-step fashion, it is more convenient to approximate the structure by tapering ω_{per} continuously, varying the diode spacings as $\tau_n = k^n\tau_0$ and the diode capacitances as $C_n = k^nC_0$ ($k < 1$) [62], [64]. Figure 28 shows the output of an NLTL soliton impulse

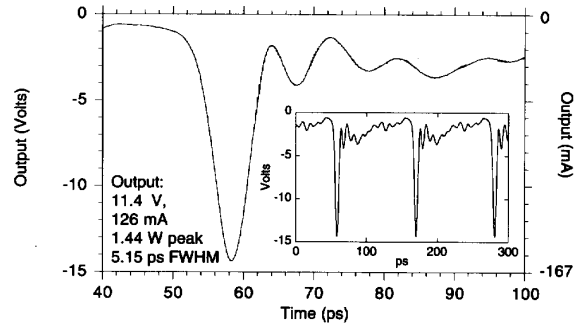compressor. Tan [64] proposed the tapered soliton impulse compressor and demonstrated compression on a scale-model device. Results with monolithic impulse compressors were first reported by Case [62], [63].

Experimental soliton NLTL output pulse durations are $\sim 7{:}1$ longer than shock-wave NLTL fall times, although circuit simulations predict attainable soliton durations only a factor of 1.5:1 longer than shock-wave NLTL fall times using similar diodes. The discrepancy is not understood. If pulse durations can be reduced, soliton compressors will be much more effective than shock-wave NLTL's for high-order millimeter-wave harmonic generation, as the conversion loss to the Nth harmonic is bounded above by $1/N$ for the soliton compressor, compared to $1/N^3$ for the shock-wave device.

IX. Traveling-Wave Resonant Tunneling-Diode Pulse Generators

Picosecond step functions can also be formed with resonant tunneling diodes (RTD's). A lumped-element RTD pulse generator (Fig. 29(a)) consists of an RTD with resistive generator and load, a circuit with bistability arising from the RTD's negative resistance [68], [69]. The RTD is a voltage-dependent current source $I(V)$ (Fig. 29(b)) with parasitic shunt capacitance C and series resistance R_s (Fig. 29(c)); in the small-signal model (Fig. 29(c)), $I(V)$ is replaced by the negative resistance R_n. The pulse-generator circuit model of Fig. 29(e) results.

As the slowly varying input voltage V_{in} increases, the device load line shifts until the current supplied to the RTD exceeds the peak current. The RTD then switches abruptly to the stable state defined by the intersection of its I–V curve and the load line (Fig. 29(b)). The rise time of this switching transition from initial voltage V_i to final voltage V_f is governed by $I = CdV/dt$, and is given by

$$T_{10\%-90\%} = \int_{0.9V_i+0.1V_f}^{0.1V_i+0.9V_f} \frac{CdV}{\Delta I(V)} \tag{23}$$

where C is the RTD capacitance and $\Delta I(V)$ (Fig. 29(b)), the difference between the RTD tunneling current and the current provided by the external circuit, is the current charging the capacitance C. Equation (23) is difficult to
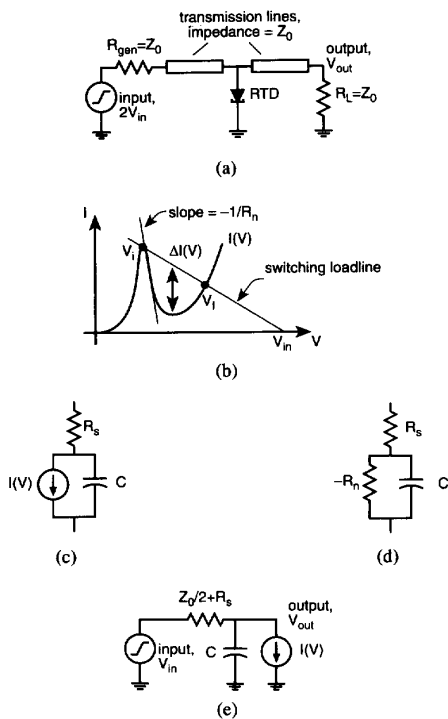
Fig. 29. Lumped-element RTD pulse generator (a), RTD current–voltage characteristics (b), large-signal (c) and small-signal (d) circuit models, and pulse generator equivalent circuit model (e).

Fig. 30. Traveling-wave RTD pulse generator circuit diagram (a), equivalent circuit (b) where $C_L = \tau_L/Z_L$ and $L = Z_L\tau_L$, and operation (c).

Fig. 31. Cross section of a Schottky-collector RTD (SRTD). In the SRTD, the top ohmic contact of the conventional RTD is replaced by a direct Schottky contact to the RTD space-charge layer, eliminating the dominant component of the parasitic series resistance.

work with, and an approximate expression for the rise time is $T_{10\%-90\%} \simeq \Delta V(C/\Delta I)$. Since the small-signal negative resistance R_n is proportional to $\Delta V/\Delta I$, the rise time $T_{10\%-90\%} \propto R_n C$.

If the RTD's quantum-well lifetime and space-charge transit time are negligible, the RTD maximum frequency of oscillation is

$$f_{max} \simeq 1/2\pi C \sqrt{R_n R_s}.$$

In the limit of small series resistance R_s, the device cutoff frequency f_{max} becomes infinite, but the rise time of the elementary RTD pulse generator of Fig. 29 does not go to zero; the circuit does not use the device efficiently. The lumped-element RTD pulse generator has the rise time determined by a capacitance charging time; once again, a distributed network should be used in order to obtain circuit performance limited by the semiconductor device f_{max}.

The corresponding distributed network, the traveling-wave RTD (TWRTD) pulse generator (Fig. 30), is a series of RTD's loading a line of impedance Z_L at electrical spacings τ_L. The equivalent circuit is shown in Fig. 30(b); a synthetic transmission line of impedance

$$Z_0 = \sqrt{L/(C + C_L)}$$

and Bragg frequency

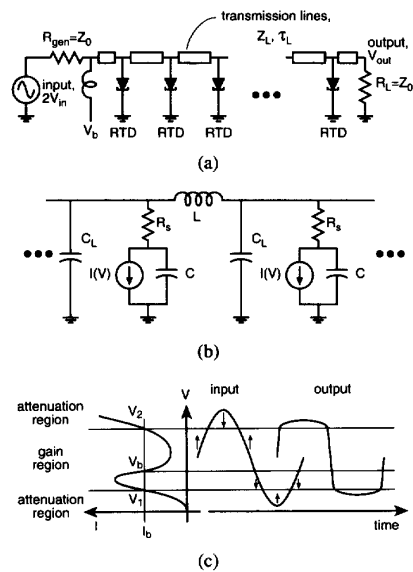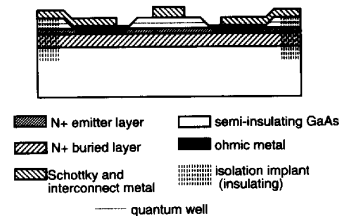$$\omega_{per} = 2/\sqrt{L(C + C_L)}$$

is formed. The TWRTD is loaded by the nonlinear shunt conductance $I(V)$.

The TWRTD has been analyzed by Ilinova [17] and Vorontsov [70]. Given bias voltage V_b and bias current I_b (Fig. 30(c)) the RTD's present a negative net resistance over the range of voltages V_1 to V_2, and thus provide gain. Outside this gain region, the RTD's present a positive net resistance, and provide attenuation. During propagation, a large-amplitude sinusoidal input signal evolves into a square wave. After a sufficient propagation distance the transition times are inversely proportional to f_{max}, with

$$T_{10\%-90\%} = (\ln 0.9 - \ln 0.1)2C\sqrt{R_n R_s} = 0.70/f_{max}$$

if $I(V)$ is approximated by a cubic polynomial in V [16], [70]. Transition times are limited by f_{max}, and the TWRTD, a distributed network, uses the RTD efficiently. TWRTD transition times will be substantially smaller than lumped-element RTD pulse generator rise times if $R_s \ll R_n$.

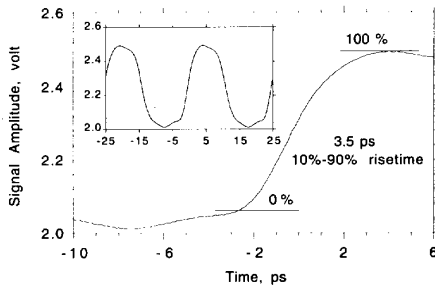Traveling-wave RTD pulse generators were fabricated using AlAs/GaAs Schottky-collector resonant tunneling

Fig. 32. Traveling-wave RTD pulse generator: measured output waveform.

Fig. 33. Measured impulse response of a GaAs Schottky photodiode with sampling circuit to a 1-ps laser pulse at a wavelength of 850 nm.

diodes (SRTD's) [71]. The SRTD (Fig. 31), is a modified RTD with the top ohmic contact and its associated n$^+$ contact layer replaced by a direct Schottky contact to the space-charge layer, thereby eliminating the associated series resistance. SRTD's have a high ratio of R_n/R_s, particularly if the Schottky contact width is reduced to submicrometer dimensions, and therefore TWRTD pulse generators using SRTD's will exhibit significantly shorter transition times than lumped-element SRTD pulse generators.

Traveling-wave RTD pulse generators have been fabricated, incorporating SRTD's with 1-μm minimum dimensions and $f_{max} \simeq 450$ GHz. Fabrication processes and circuit layouts are almost identical to those used for the NLTL. Figure 32 shows the TWRTD output measured by an NLTL-based active wafer probe (Section X-B); with a 40-GHz, 3-V peak–peak input, a 3.5-ps transition time is measured. Performance of the present monolithic device is *seriously* degraded by transmission-line losses arising from poor cell layout. With reduced transmission-line losses and with 0.1-μm Schottky-contact width SRTD's having $f_{max} \sim 900$ GHz [71], subpicosecond TWRTD transition times should be attainable.

X. APPLICATIONS

Demonstrated applications include integrated photodetectors and sampling circuits for optical waveform measurements and systems for millimeter-wave network analysis both on-wafer and in free space.

A. Monolithic Photodiode/Sampling Circuit

In conjunction with sampling oscilloscopes, high-speed photodetectors provide measurements of optical waveforms occurring in fiber-optic transmission systems and optoelectronic devices. By adding a single process step for semitransparent Schottky contacts, GaAs Schottky photodetectors can be integrated with the sampling circuits for direct measurements of picosecond optical waveforms [24]. The monolithic photodiode/sampling circuit [24] combines a photodetector and an NLTL-based sampling circuit (Fig. 33); illuminated by 1-ps pulses from a $\lambda = 850$-nm dye laser, a 5.6-ps FWHM impulse response (Fig. 33) is observed. Ozbay [25] has reported monolithic photodetector/sampling circuits with a combined 2.0-ps impulse response at $\lambda = 532$-nm illumination.

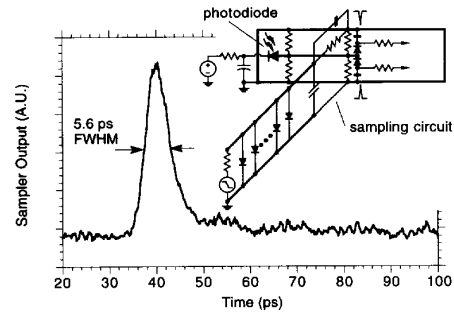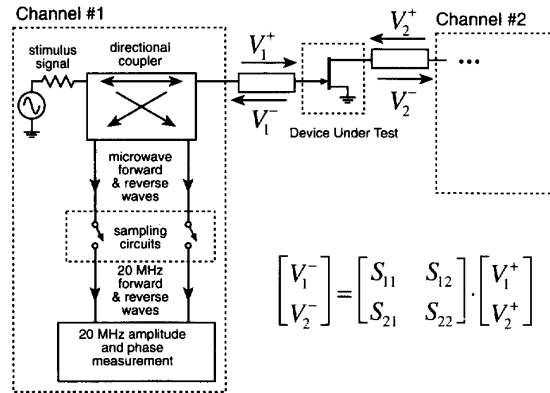Fig. 34. Simplified block diagram of a typical microwave network analyzer. Channel no. 2 is identical to channel no. 1. Network analyzers measure the wave scattering matrix S_{ij}, as defined in the figure.

B. On-Wafer Millimeter-Wave Network Analysis

Transistor power-gain cutoff frequencies have exceeded 450 GHz [31], [32], enabling demonstration of monolithic 120-GHz amplifiers. For circuit development at higher frequencies, improvements in transistor bandwidth must be accompanied by development of the wideband instrumentation used both for device modeling and for circuit evaluation.

A vector network analyzer (VNA) measures as a function of frequency the two-port characteristics of a device under test. Microwave device characteristics are traditionally described by the wave scattering matrix (S parameters), which gives the relationship between the incident and emanating waves on 50-Ω transmission lines connected to the device. Circuit models are obtained by fitting model element values to the measured scattering parameters.

In a typical microwave network analyzer (Fig. 34), a swept-frequency signal generator drives the device under test. The incident and reflected waves are separated by a directional coupler, downconverted to radio frequencies by sampling circuits, and subsequently measured. Bandwidth limits include the sampling circuits and the frequency
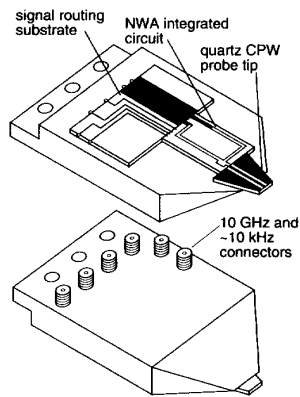
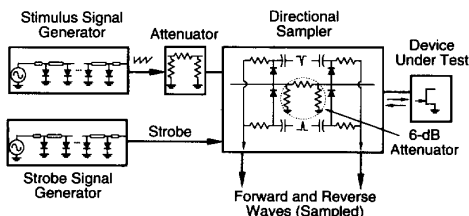**Fig. 35.** Active probe for on-wafer millimeter-wave network analysis.

Fig. 36. Block diagram of the network analysis integrated circuit.

Fig. 37. Network analysis system using active probes.

range of the stimulus signal generator. Coaxial connectors also limit bandwidth; 110-GHz coaxial connectors were introduced in March 1993, with earlier connectors limited to 65 GHz.

Active probes [20], [72], [73] (Fig. 35) have been developed for on-wafer millimeter-wave vector network analysis to 200 GHz. These contain a network analyzer IC and a rugged, wideband quartz probe tip. The IC itself incorporates an NLTL stimulus signal generator and an NLTL-strobed directional sampling circuit which independently measures the forward and reverse waves from the device under test.

The network analyzer IC block diagram is shown in Fig. 36 and the measurement system in Fig. 37. An NLTL stimulus signal generator converts an $f_0 = 7$–14 GHz sinusoidal drive signal into a 5-V sawtooth waveform with $\sim$ 2.5-ps transition times and with significant power at harmonics nf_0 as high as 250 GHz. The drive signal is attenuated to levels suitable for linear characterization of transistor circuits, and is passed through a directional sampling circuit to the device under test.

The directional sampling circuit is a pair of sampling circuits measuring the port voltages of a 6-dB attenuator placed between the stimulus signal generator and the device under test. A second NLTL on the IC provides the strobe signal for the directional sampling circuit. The attenuator port voltages $V_{out} = V^+ + V^-$ and $V_{in} = 2V^+ + V^-/2$, linear functions of the incident and reflected voltages V^+ and V^-, are downconverted by the sampling circuits to a $\Delta f =$
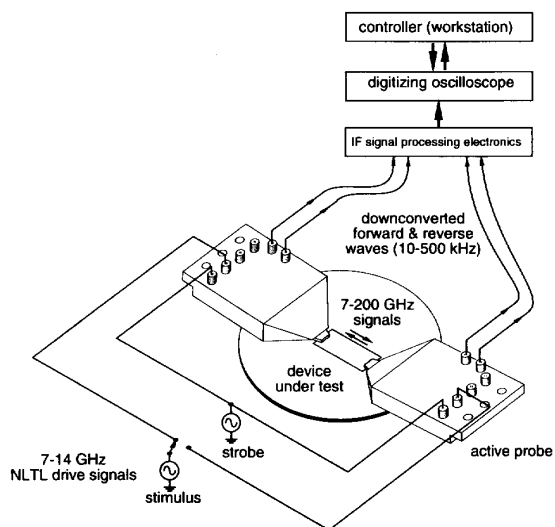
20 kHz intermediate frequency, with the nth harmonic of the signal frequency f_0 begin downconverted to an IF frequency $n\Delta f$. The IF signals are passed through summing networks to recover V^+ and V^-, and are then measured by a digitizing oscilloscope. A computer controller computes the Fourier series of the measured waveforms to determine the vector amplitudes of the signal harmonics at $n\Delta f$. The active probes are first calibrated by measuring a series of known calibration standards.

To minimize high-frequency losses, the probe tips are short (2 mm), and are fabricated on quartz substrates, a material whose low dielectric constant results in low (0.6 dB/mm at 200 GHz) attenuation. The probe tips have nickel contact points and airbridge ground straps for parasitic CPS mode suppression. The 60-pH wire-bond inductance between the probe tip and the network analyzer IC is acceptable for 200-GHz measurements.

Errors arise in network analysis both from the instrument and from the calibration standards themselves. To determine the instrument accuracy, the NWA is first calibrated and the calibration standards are subsequently re-measured. The deviation between the measurement and the standard's specified characteristics is the instrument error. Figure 38 shows the characteristics of a through-line calibration standard from 8 to 200 GHz, measured 30 min after calibration. Except near 200 GHz, deviation from the expected S-parameters is much less than 1 dB in amplitude and 0.1 ps in delay. Presently, the calibration standards are unverified above 100 GHz, and errors in the standards result in $\sim$ 1-dB errors in measured reflection magnitudes above 100 GHz.

Figure 39 shows the forward gain (S_{21}), measured by the active probes, of a HEMT distributed amplifier provided by J. Braunstein of the Fraunhofer Institute [74]. Directional sampling circuits were first reported by Marsland [58], and Shakouri [22] has demonstrated waveform measurements with 0.88-ps rise time using active probes.
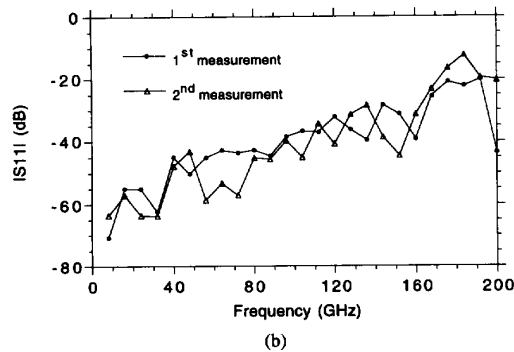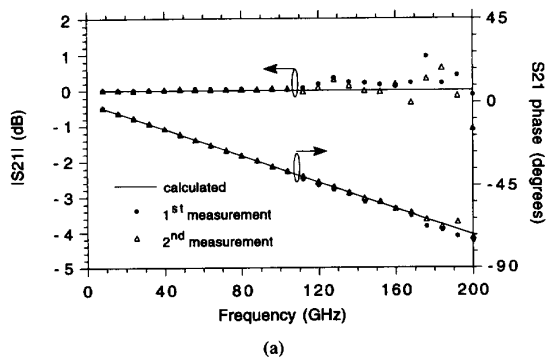
Fig. 38. Measured transmission magnitude and phase (a) and reflection magnitude (b) of a 1-ps length through-line calibration standard. Instrument error is indicated by the deviation of S_{21} from 0 dB and 1-ps delay (solid lines) and the deviation of S_{11} from zero ($-\infty$ dB).
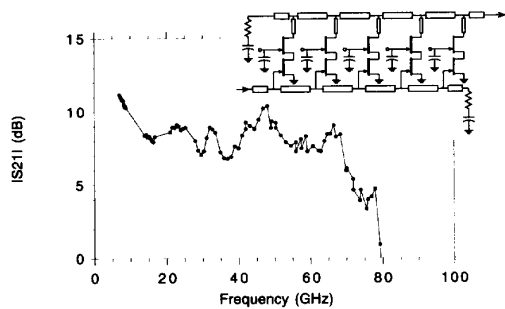

Fig. 39. Forward gain S_{21}, measured by the active probe, of a HEMT distributed amplifier provided by J. Braunstein, Fraunhofer Institute [74].

C. Free-Space Network Analysis

NLTL's and sampling circuits can also be used for gain–frequency measurements in free space [21], [29], for characterization of materials and quasi-optical array amplifiers [75]. As with the on-wafer measurement system, the system generates and detects picosecond pulses and obtains frequency information through computing the Fourier series of the received signal.

For broadband measurements, the NLTL and sampling circuits must be interfaced to broadband antennas. The bow-tie antenna is scale-invariant and has a frequency-independent radiation impedance and a
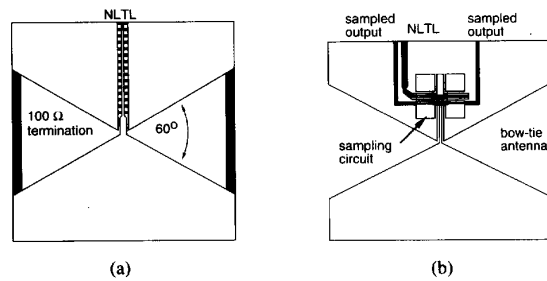
Fig. 40. Simplified integrated circuit layouts of (a) picosecond transmitter and (b) picosecond receiver.
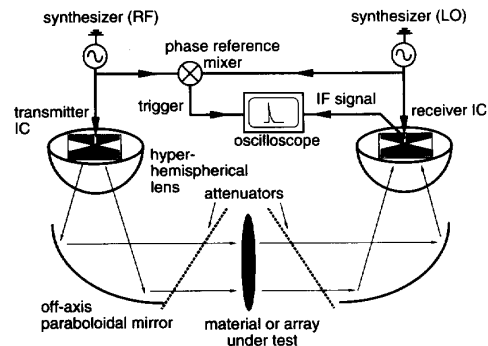
Fig. 41. Free-space measurement system schematic diagram.

frequency-independent far-field radiation pattern [46]. The transmitter NLTL, fabricated within one electrode plane, drives the 50-Ω impedance antenna (Fig. 40(a)). The receiver is a bow-tie antenna interfaced to an sampling circuit (Fig. 40(b)). The NLTL output is radiated through the substrate and partially collimated by a high-resistivity silicon substrate lens (Fig. 41) [46]. The radiated beam is collimated with off-axis parabolic mirrors, and is focused on the receiver through similar optics. Cavity resonances between the transmitter and receiver are suppressed by placing 5-dB attenuators at oblique incidence on both sides of the sample under test. Van Der Weide [23] has reported a similar system.

The transmitter NLTL is driven between 7 and 14 GHz, while the sampling circuit is driven at a frequency 100 Hz below the transmitter frequency. The resulting sampled 100-Hz signal is observed directly on an oscilloscope. The received signal is a pulse train with 2.4-ps rise time. Attenuation-frequency measurements are obtained by taking the ratio of the received Fourier series with the device under test in place with the Fourier series of a reference measurement taken with the device under test removed. Figure 42 shows a measurement of a high-Q Bragg filter.

D. Multiplexers for Fiber-Optic Transmission

NLTL's and sampling circuits have applications beyond the area of instrumentation. To cite one example, NLTL-based multiplexer and demultiplexer circuits for fiber-optic data transmission at 100-Gb/s rate are currently being developed. 100-Gb/s transmission is a substantial challenge, but many of the component technologies are now
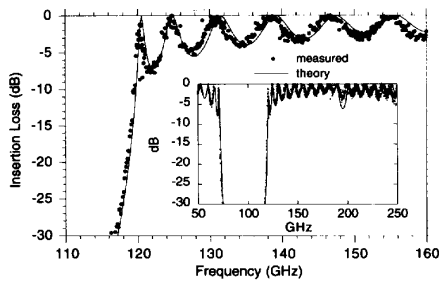
Fig. 42. Measured transmission magnitude for a 9.5-period Alumina–Teflon Bragg filter. The system also measures transmission phase.
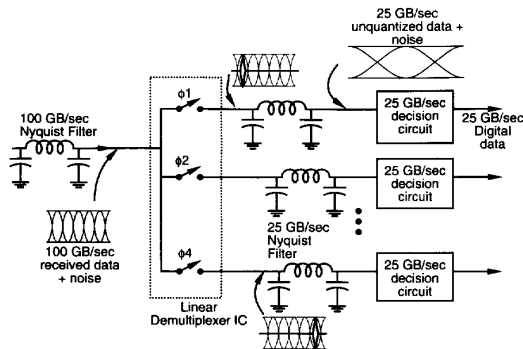

Fig. 43. NLTL-based demultiplexer for 100-Gb/s fiber-optic data transmission.

in place. Long-wavelength photodetectors [76] and HEMT distributed amplifiers [34], [74] have sufficient bandwidth for this application, while electrooptic modulators need only moderate improvements in bandwidth [45]. Optical fiber dispersion can be counteracted by dispersion compensation or by optical soliton propagation [53], and erbium-doped fiber preamplifiers will provide adequate receiver signal/noise ratio [77]. 100-Gb/s multiplexing is problematic.

Reported 27-Gb/s transistor multiplexers and decision circuits [78] should shortly evolve to 40-Gb/s rates, but multiplexing and demultiplexing at 100 Gb/s with current transistors appears to be very difficult. NLTL technology provides an alternative (Fig. 43). Received 100-Gb/s data in the presence of noise are passed through a 100-Gb/s Nyquist filter (a high-order 50-GHz low–pass filter). The signal is passed through a linear demultiplexer IC consisting of four synchronized sampling gates clocked by a 25-GHz, 4-phase clock ($\phi_1-\phi_4$), generating four parallel unquantized data streams. Each data stream is passed through a 25-Gb/s Nyquist filter to a transistor decision circuit, where the signal is quantized and resynchronized. A similar system is used for multiplexing.

The demultiplexer's sampling gates are diode bridges gated by NLTL's. Unlike sampling circuits, where the sampled (IF) bandwidth is low, the demultiplexer gates must provide a 25-Gb/s output and a four-diode or six-diode

bridge is consequently required. The required aperture time for a 100-Gb/s multiplexer IC is relatively large, $\sim$ 5 ps, nearly an order of magnitude larger than that attained by NLTL-gated sampling circuits.

XI. CONCLUSION

Applications for electronics above 100 GHz will emerge. Many applications, including pulse-code data transmission and instrumentation, are broadband and thus incompatible with resonant circuit designs. Distributed circuits provide efficient use of semiconductor devices over broad bandwidths and will serve these broadband applications. Established distributed devices include traveling-wave amplifiers and electrooptic modulators. Nonlinear distributed circuits use very wideband Schottky diodes for step-function and impulse generation though shock-wave formation and soliton decomposition. These have had significant impact on high-speed instrumentation.

Microwave instruments have not kept pace with advances in high-frequency transistors. Without instruments for device characterization and circuit evaluation, monolithic circuit development is difficult, and progress is impeded. Shock-wave NLTL's generate subpicosecond pulses and have enabled development dc–700 GHz sampling circuits. For subpicosecond pulse generation, traveling-wave Schottky-collector RTD's may compete with NLTL's. Experimental instruments using NLTL's have demonstrated waveform and network measurements over several hundred gigahertz bandwidths. Commercial instruments using NLTL's are now available [56], [57]. NLTL applications in wideband communications and signal processing will also emerge.

ACKNOWLEDGMENT

REFERENCES

[1] R. S. Kirkby, S. Withington, A. B. Darling, and F.G. Kilgour, *Engineering in History.* New York: McGraw-Hill, 1956.
[2] R. Heidemann, B. Wedding, and G. Veith, "10 Gb/s transmission and beyond," *Proc. IEEE*, vol. 81, no. 11, pp. 1558–1567, Nov. 1993.
[3] H. G. J. Aitken, *Syntony and Spark—The Origins of Radio.* New York: Wiley-Interscience, 1976.
[4] W. M. Dalton, *The Story of Radio* (in 3 parts). London, UK: Adam Hilger, 1975.
[5] W. R. Maclaurin and R. J. Harman, *Invention and Innovation in the Radio Industry.* New York: MacMillan, 1949.
[6] S. S. Swords, *Technical History of the Beginnings of Radar.* London, UK: Peter Peregrinus, 1986.
[7] J. W. Waters, "Submillimeter-wavelength heterodyne spectroscopy and remote sensing of the upper atmosphere," *Proc. IEEE*, vol. 80, no. 11, Nov. 1992.
[8] T. W. Crowe, R. J. Mattauch, H. P. Röser, W. L. Bishop, W. C. B. Peatman, and X. Liu, "GaAs Schottky diodes for THz mixing

applications," *Proc. IEEE*, vol. 80, no. 11, pp. 1827–1841, Nov. 1992.

[9] M. J. W. Rodwell, M. Kamegawa, R. Yu, M. Case, E. Carman, and K. Giboney, "GaAs nonlinear transmission lines for picosecond pulse generation and millimeter-wave sampling," *IEEE Trans. Microwave Theory Tech.*, vol. 39, no. 7, pp. 1194–1204, July 1991.

[10] R. L. Fork, C. H. Brito-Cruz, P. C. Becker, and C. V. Shank, *Opt. Lett.*, vol. 12, p. 483, 1987.

[11] A. Yariv and P. Yeh, *Optical Waves in Crystals*. New York: Wiley-Interscience, 1984.

[12] R. Landauer, "Parametric amplification along nonlinear transmission lines," *J. Appl. Phys.*, vol. 31, no. 3, pp. 479–484, 1960.

[13] R. Landauer, "Shock waves in nonlinear transmission lines and their effect on parametric amplification," *IBM J. Res. Devel.*, vol. 4, no. 4, pp. 391–401, Oct. 1960.

[14] A. C. Scott, F. Y. F. Chu, and D. W. McLaughlin, "The soliton: A new concept in applied science," *Proc. IEEE*, vol. 61, no. 10, pp. 1443–1482, Oct. 1973.

[15] R. Hirota and K. Suzuki, "Theoretical and experimental studies of lattice solitons in nonlinear lumped networks," *Proc. IEEE*, vol. 61, no. 10, pp. 1483–1491, Oct. 1973.

[16] R. V. Khokhlov, "On the theory of shock radio waves in nonlinear lines," *Radiotekhn. Elektron.*, vol. 6, no. 6, pp. 917–925, 1961.

[17] T. M. Il'inova and R. V. Khokhlov, "Wave processes in lines with nonlinear shunt resistance," *Radiotekhn. Elektron.*, vol. 8, pp. 1864–1872, 1963.

[18] A. Scott, *Active and Nonlinear Wave Propagation in Electronics*. New York: Wiley-Interscience, 1970.

[19] E. Carman, M. Case, M. Kamegawa, R. Yu, K. Giboney, and M. J. W. Rodwell, "V-band and W-band broadband, monolithic distributed frequency multipliers," *IEEE Microwave Guided-Wave Lett.*, vol. 2, no. 6, pp. 253–254, June 1992.

[20] R. Yu, M. Reddy, J. Pusl, S. Allen, M. Case, and M. Rodwell, "Full two-port on-wafer vector network analysis to 120 GHz using active probes," in *Dig. 1993 IEEE Int. Microwave Symp.* (Atlanta, GA, June, 1993).

[21] Y. Konishi, M. Kamegawa, M. Case, R. Yu, M. J. W. Rodwell, and D. B. Rutledge, "Picosecond spectroscopy using monolithic GaAs circuits," *Appl. Phys. Lett.*, vol. 61, no. 23, p. 7, Dec. 1992.

[22] M. S. Shakouri, A. Black, B. A. Auld, and D. M. Bloom, "500 GHz MMIC sampling wafer probe," *Electron. Lett.*, vol. 29, no. 6, pp. 557–558, Mar. 18, 1993.

[23] D. W. Van Der Weide, J. S. Bostak, B. A. Auld, and D. M. Bloom, "All-electronic generation of 880 fs, 3.5 V shockwaves and their application to a 3 THz free-space signal generation system," *Appl. Phys. Lett.*, vol. 58, pp. 222–224, 1991.

[24] M. Kamegawa, K. Giboney, J. Karin, M. Case, R. Yu, M. J. W. Rodwell, and J. E. Bowers, "Picosecond GaAs monolithic optoelectronic sampling circuit," *IEEE Photonics Technol. Lett.*, vol. 3, no. 6, pp. 567–569, June 1991.

[25] E. Ozbay, K. D. Li, and D. M. Bloom, "2.0 ps, 150 GHz monolithic photodiode and all-electronic sampler," *IEEE Photonics Technol. Lett.*, vol. 3, no. 6, pp. 570–572, June 1991.

[26] U. D. Keil and D. R. Dykaar, "Electrooptic sampling at 150 fs," in *Proc. 1993 OSA Conf. on Ultrafast Electronics and Optoelectronics* (San Francisco, CA, Jan. 25–27).

[27] D. H. Auston, "Impulse response of photoconductors in transmission lines," *IEEE J. Quantum Electron.*, vol. 19, no. 4, Apr. 1983

[28] J. Nees, S. Williamson, J. Kim, and S. Gupta, "Picosecond detector, optical temporal analyzer, and free-standing circuit probe," proceedings, 1993 OSA conference on Ultrafast Electronics and Optoelectronics, San Francisco, CA, Jan. 25–27.

[29] N. Katzenellenbogen and D. R. Grischkowsky, "Efficient generation of 380 fs pulses of THz radiation by ultrafast laser pulse excitation of a biased metal-semiconductor interface," *Appl. Phys. Lett.*, vol. 58, no. 3, pp. 222–224, Jan. 1991.

[30] J. A. Valdmanis, G. Mourou, and C. W. Gabel, "Picosecond electrooptic sampling system," *Appl. Phys. Lett.*, vol. 41, pp. 211–212, 1982.

[31] L. D. Nguyen, A. S. Brown, M. A. Thompson, L. M. Jelloian, L. E. Larson, and M. Matloubian, "650-Å self-aligned-gate pseudomorphic $Al_{0.48}In_{0.52}As/\ Ga_{0.20}In_{0.80}As$ high electron mobility transistors," *IEEE Electron Device Lett.*, vol. 13, no. 3, pp. 143–145, Mar. 1992.

[32] P. Ho, M. Y. Kao, P. C. Chao, K. H. G. Duh, J. M. Ballinger, S. T. Allen, A. J. Tessmer, and P. M. Smith, "Extemely high gain 0.15 μm gate-length InAlAs-/InGaAs/InP HEMTs," *Electron. Lett.*, vol. 27, no. 4, pp. 325–327, Feb. 14, 1991.

[33] H. Wang, T. N. Ton, K. L. Tan, D. Garske, G. S. Dow, J. Berenz, M. W. Popieszalski, and S. K. Pan, "A D-band monolithic low-noise amplifier," in *Proc. 1992 IEEE GaAs IC Symp.* (Miami Beach, FL, Oct. 4–7).

[34] R. Madjidi-Ahy, C. K. Nishimoto, M. Riaziat, M. Glenn, S. Silverman, S.-L. Weng, Y.-C. Pao, G. A. Zdasiuk, S. G. Bandy, and Z. C. Tan, "5–100 GHz InP coplanar waveguide MMIC distributed amplifier," *IEEE Trans. Microwave Theory Tech.*, vol. 38, no. 12, pp. 1986–1993, Dec. 1990.

[35] H.-P. Röser, "Heterodyne spectroscopy for submillimeter and far—Infrared wavelengths from 100 μm to 500 μm," *Infrared Phys.*, vol. 32, pp. 385–407, 1991.

[36] H. Rothermel, T. G. Phillips, and J. Keene, "A solid-state frequency source for radio astronomy in the 100 to 1000 GHz range," *Int. J. Infrared Millimeter Waves*, vol. 10, no. 1, pp. 83–100, 1989.

[37] E. R. Brown, J. R. Söderström, C. D. Parker, L. J. Mahoney, K. M. Molver, and T. C. McGill, "Oscillations up to 712 GHz in InAs/AlSb resonant-tunneling-diodes," *Appl. Phys. Lett.*, vol. 58, no. 20, pp. 2291–2293, May 20, 1991.

[38] G. D. Vendelin, *Design of Amplifiers and Oscillators by the S-Parameter Method*. New York: Wiley-Interscience, 1982.

[39] R. M. Fano, "Theoretical limitations on the broadband matching of arbitrary impedances," *J. Franklin Inst.*, vol. 249, pp. 57–83, Jan. 1960; and pp. 139–155, Feb. 1960.

[40] W. S. Percival, British Patent Specification No. 460, 562, applied for July 24, 1936.

[41] E. L. Ginzton, W. R. Hewlett, J. H. Jasberg, and J. D. Noe, "Distributed amplification," *Proc. IRE*, vol. 36, pp. 956–969, Aug. 1948.

[42] Y. Ayasli, R. L. Mozzi, J. L. Vorhaus, L. D. Reynolds, and R. A. Pucel, "A monolithic GaAs 1-13 GHz traveling-wave amplifier," *IEEE Trans. Microwave Theory Tech.*, vol. 30, no. 7, pp. 976–981, July 1982.

[43] K. S. Giboney, M. J. W. Rodwell, and J. E. Bowers, "Travelling-wave photodetectors," *Photonics Technol. Lett.*, vol. 4, no. 12, pp. 1363–1365, Dec. 1992.

[44] J. R. Pierce and L. M. Field, "Traveling-wave tubes," *Proc. IRE*, vol. 35, pp. 108–111, Feb. 1947.

[45] R. G. Walker, "High-speed III-V semiconductor intensity modulators," *IEEE J. Quantum Electron.*, vol. 27, no. 3, pp. 654–667, Mar. 1991.

[46] D. B. Rutledge, D. P. Neikirk, and D. P. Kasilingam, " Integrated-circuit antennas" in *Infrared and Millimeter Waves*, vol. 10, K. J. Button, Ed. New York: Academic Press, 1984, pp. 1–90.

[47] R. Hoffmann, *Handbook of Microwave Integrated Circuits*. Norwood, MA: Artech House, 1987.

[48] W. Bascom, *Waves and Beaches*. New York: Anchor Press/Doubleday, 1980.

[49] R. P. Feynman, R. B. Leighton, and M. Sands, *The Feynman Lectures on Physics*, vol. 1. Reading, MA: Addison-Wesley, 1963, ch. 51.

[50] E. Infeld and G. Rowland, *Nonlinear Waves, Solitons, and Chaos*. Cambridge, UK: Cambridge Univ. Press, 1990.

[51] D. J. Korteweg and G. deVries, "On the change of form of long waves advancing in a rectangular canal, and on a new type of long stationary waves," *Phil. Mag.*, vol. 39, pp. 422–443, 1895.

[52] N. J. Zabusky and M. D. Kruskal, "Interaction of solitons in a collisionless plasma and the recurrence of initial states," *Phys. Rev. Lett.*, vol. 15, pp. 240–243, 1965.

[53] H. Haus, "Optical fiber solitons, their properties and uses," *Proc. IEEE*, vol. 81, no. 7, pp. 970–983, July 1993.

[54] J. L. Moll and S. A. Hamilton, "Physical modeling of the step recovery diode for pulse and harmonic generation circuits," *Proc. IEEE* , vol. 57, no. 7, pp. 1250–1259, July 1969.

[55] W. M. Grove, "Sampling for oscilloscopes and other RF systems, dc through X-band," *IEEE Trans. Microwave Theory Tech.*, vol. MTT-14, no. 12, pp. 629–635, Dec. 1966.

[56] Hewlett-Packard Co., "HP54124T 50 GHz digitizing oscilloscope," Tech. Rep. ,5301 Stevens Creek Blvd., Santa Clara, CA.

[57] W. C. Whitely, W. E. Kuntz, and W. J. Anklam, "50 GHz sampler hybrid using a small shockline and an internal SRD," in *Proc. 1991 IEEE MTT-S Int. Microwave Symp.*, pp. 895–898, 1991.

[58] R. A. Marsland, C. J. Madden, D. W. Van Der Weide, M. S. Shakouri, and D. M. Bloom, "Monolithic integrated circuits for millimeter-wave instrumentation," in *Proc. 1990 IEEE GaAs IC Symp.* (New Orleans, LA, Oct. 7–10), pp. 19–22.

[59] S. T. Allen, U. Bhattacharya, and M. J. W. Rodwell, "4 THz sidewall-etched varactors for sub-mm-wave sampling circuits," in *Proc. 1993 IEEE GaAs IC Symp.* (San Jose, CA, Oct. 1993).

[60] R. A. Marsland, V. Valdivia, C. J. Madden, M. J. W. Rodwell, and D. M. Bloom, "130 GHz GaAs monolithic integrated circuit sampling head," *Appl. Phys. Lett.*, vol. 55, no. 6, Aug. 7, 1989.

[61] R. Yu, M. Case, M. Kamegawa, M. Sundaram, M. J. W.Rodwell, and A. Gossard, "275 GHz 3-mask integrated GaAs sampling circuit," *Electron. Lett.*, vol. 26, no. 13, pp. 949–951, June 21, 1990.

[62] M. Case, M. Kamegawa, R. Yu, M. J. W. Rodwell, and J. Franklin, "Impulse compression using soliton effects in a monolithic GaAs circuit," *Appl. Phys. Lett.*, vol. 58, no. 2, pp. 173–175, Jan. 14, 1991.

[63] M. Case, E. Carman, R. Yu, and M. J. W. Rodwell, "Picosecond duration, large-amplitude impulse generation using electrical soliton effects," *Appl. Phys. Lett.*, vol. 60, no. 24, pp. 3019–3021, June 15, 1992.

[64] M. Tan, C. Y. Su, and W. J. Anklam, "7 X electrical pulse compression on an inhomogenous nonlinear transmission line," *Electron. Lett.*, vol. 24, no. 4, pp. 213–215, Feb. 18, 1988.

[65] E. Carman, K. Giboney, M. Case, M. Kamegawa, R. Yu, K. Abe, M. Rodwell, and J. Franklin, "28–39 GHz distributed harmonic generation on a soliton nonlinear transmission line," *IEEE Microwave and Guided-Wave Lett.*, vol. 1, no. 2, pp. 28–31, Feb. 1991.

[66] R. A. Marsland, M. S. Shakouri, and D. M. Bloom, "Millimeter-wave generation on a nonlinear transmission line," *Electron. Lett.*, vol. 26, no. 16, pp. 1235–1236, 1990.

[67] K. S. Champlin and D. R. Singh, "Small-signal second-harmonic generation by a nonlinear transmission line," *IEEE Trans. Microwave Theory Tech.*, vol. MTT-34, no. 3, pp. 351–353, Mar. 1986.

[68] S. K. Diamond, E. Özbay, M. J. W. Rodwell, D. M. Bloom, Y. C. Pao, and J. S. Harris, "Resonant tunneling diodes for switching applications," *Appl. Phys. Lett.*, vol. 54, no. 2, pp. 153–155, Jan. 9, 1989.

[69] E. Ozbay, D. M. Bloom, D. H. Chow and J. N. Schulman, "1.7 ps, microwave integrated-circuit-compatible InAs/AlSb resonant tunneling diodes," *IEEE Electron Device Lett.*, vol. 14, no. 8, 1993.

[70] Y. I. Vorontsov, "Certain properties of delay lines containing tunnel diodes," *Radiotekh. Elektron.*, vol. 9, no. 4, pp. 478–483, 1964.

[71] S. T. Allen, M. Reddy, M. J. W. Rodwell, R. P. Smith, J. Liu, S. C. Martin, and R. E. Muller, "Submicron Schottky-collector AlAs/GaAs resonant tunnel diodes," in *IEDM Tech. Dig.*(Washington DC, Dec. 1993).

[72] R. Yu, M. Kamegawa, M. Case, M. Rodwell, and J. Franklin, "A 2.3 ps time-domain reflectometer for millimeter-wave network analysis," *IEEE Microwave Guided-Wave Lett.*, vol. 1, no. 11, pp. 334–336, Nov. 1991.

[73] R. Yu, J. Pusl, Y. Konishi, M. Case, M. Kamegawa, and M. Rodwell, "A time-domain millimeter-wave vector network analyzer," *IEEE Microwave Guided Wave Lett.*, vol. 2, no. 8, pp. 319–321, Aug. 1992.

[74] J. Braunstein, M. Schlechtweg, P. L. Tasker, W. Reinert, A. Julsmann, K. Hohler, W. Bronner, R. Bosch, and W. Haydl, "High performance narrow and wide bandwidth amplifiers in CPW-technology up to W-band," in *Tech. Dig. 1993 IEEE GaAs IC Symp.* (San Jose, CA, Oct. 10–13).

[75] R. M. Weikle II, M. Kim, J. B. Hacker, M. P. De Lisio, Z. B. Popović, and D. B. Rutledge, "Transistor oscillator and amplifier grids," *Proc. IEEE*, vol. 80, no. 11, pp. 1800–1809, Nov. 1992.

[76] Y.-G. Wey, K. Giboney, J. Bowers, M. Rodwell, P. Silvestre, P. Thiagarajan, and G. Robinson, "110 GHz GaInAs/InP p-i-n photodiodes with integrated bias tees and matched resistors" *IEEE Photonics Technol. Lett.*, vol. 5, no. 11, Nov. 1993.

[77] T. Li, "The impact of optical amplifiers on long-distance lightwave telecommunications," *Proc. IEEE*, pp. 1568–1580, vol. 81, no. 11, Nov. 1993.

[78] K. Runge, D. Daniel, J. L. Gimlett, R. B. Nubling, R. L. Pierson, M. F. Chang, K. C. Wang and D. M. Chen, "A 27 Gb/sec HBT 4:1 multiplexer IC," in *Tech. Dig. IEEE GaAs IC Symp.* (Monterery, CA, Oct. 20–23, 1991).
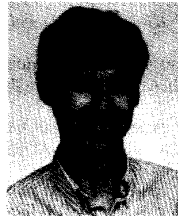
Mark J. Rodwell (Member, IEEE) was born in Altrincham, Cheshire, England, on January 18, 1960. He received the B.S. degree in electrical engineering from the University of Tennessee, Knoxville, in 1980, and the M.S. degree from Stanford University, Stanford, CA, in 1982. He received the Ph.D. degree in electrical engineering also from Stanford University in 1988.

From 1981 through 1984 he worked for AT&T Bell Laboratories, developing optical transmission systems. He was a research associate at Stanford University from January to September 1988, when he joined the Department of Electrical and Computer Engineering, University of California, Santa Barbara., and is currently an Associate Professor there. His research involves picosecond electrical shock-wave and soliton devices, millimeter-wave generation and instrumentation, picosecond photodetectors, fiber-optic transmission technologies, resonant tunneling diodes, and millimeter-wave HBT and HEMT circuit design. He is the recipient of a 1989 National Science Foundation Presidential Young Investigator Award.
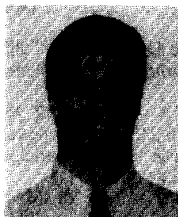
Scott T. Allen received the B.S. degree in electrical engineering from Cornell University, Ithaca, NY, in 1987, and the M.S. degree from the University of Massachusetts, Amherst, in 1989,

From 1987 to 1990 he worked at the Martin Marietta Electronics Laboratory in Syracuse, NY, where he was involved with HEMT device modeling and millimeter-wave circuit design. Since 1990 he has been pursuing the Ph.D. degree in electrical engineering at the University of California, Santa Barbara, where his research has been in the areas of compound semiconductor devices and submillimeter wave integrated circuits.
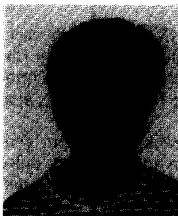
Ruai Y. Yu received the B.S. degree in electrical engineering from San Francisco State University, San Francisco, CA, in 1988, and the M.S. as well as Ph.D. degrees, both in electrical engineering, from the University of California at Santa Barbara in 1991 and 1994, respectively.

From 1988 to 1989, he was a research engineer at Ampex Corporation, where he engaged in the research and development of advanced equalization schemes for high-speed digital recording channels. While a graduate student at UCSB, he worked on monolithic and hybrid integrated circuits for microwave/millimeter-wave waveform and network measurements. He is currently a Member of Technical Staff in High Speed Circuits Department, Rockwell International Science Center, where he is involved in the design and packaging of MMIC's for high bit rate optical transmission systems.

Michael G. Case was born in Ventura, CA, in 1966. He received the B.S. degree in 1989, the M.S. degree in 1991, and the Ph.D. degree in 1993, all from the University of California, Santa Barbara.

He did graduate research supported by a State Fellowship. His Ph.D. research concerned nonlinear transmission lines for applications in high-speed waveform shaping and signal detection. Since 1993 he has been with Hughes Aircraft Company Research Laboratories, Malibu, CA, where he is involved with two- and three-terminal device design and process development, high-speed circuit design, and measurement techniques.
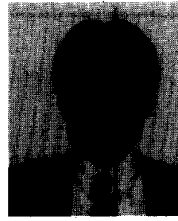
Masayuki Kamegawa was born in Shiga, Japan, on September 27, 1958. He received the B.S. and M.S. degrees in applied physics from Osaka University, Osaka, Japan, in 1982 and 1984, respectively.

He joined the Shimadzu Corporation, Kyoto, Japan, in 1984, where he developed a semiconductor X-ray detector for medical imaging systems. He was a visiting scientist at the University of California, Santa Barbara, from 1989 to 1991, and engaged in research on application of nonlinear transmission lines and high-speed samplers. He is currently working in research and development of semiconductor lasers and their applications at Shimadzu Corporation, Keihanna Laboratories, Kyoto.
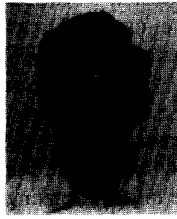
Uddalak Bhattacharya received the B. Tech. degree in electronics and electrical communication engineering from the Indian Institute of Technology, Kharagpur, India, in 1991, and the M.S. degree in electrical engineering from the University of California at Santa Barbara in 1993.

He is currently pursuing the Ph.D. degree at the University of California at Santa Barbara. His research focuses on developing nonlinear transmission line technologies and applications. He is also working on high-speed circuits for terahertz applications.

Yoshiyuki Konishi was born in Hyogo, Japan, on February 16, 1965. He received the B.S. and M.S. degrees in applied physics from Osaka University, Osaka, Japan, in 1987 and 1989, respectively.

He joined the Shimadzu Corporation, Kyoto, Japan, in 1989, where he developed a high-voltage generator for accelerators used in high-energy ion-beam analysis. He was a visiting scientist at the University of California, Santa Barbara, from 1991 to 1993, and engaged in research on application of nonlinear transmission lines for millimeter-wave spectroscopy and on development of Schottky-collector resonant tunneluing diodes. He is currently working on research and development of high-energy ion-beam analysis and implementation at Shimadzu Corporation, Keihanna Laboratories, Kyoto.
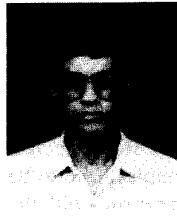
Madhukar Reddy was born in Hyderabad, India, on November 4, 1969. He received the B. Tech. degree in electronics and communication engineering from the Indian Institute of Technology, Madras, India, in 1991, and the M.S. degree in electrical engineering from the University of California, Santa Barbara, in 1993.

He is currently pursuing the Ph.D. degree in electrical engineering at the University of California, Santa Barbara. His current research focuses on developing terahertz resonant tunnel diodes and terahertz oscillators.

Joe Pusl was born in San Diego, CA, on September 19, 1968. He received the B.S. degree in 1990 and the M.S. degree in 1992 in electrical engineering, both from the University of California, Snata Barbara.

While pursuing the M.S. degree, he worked under Dr. Rodwell on broadband millimeter-wave MMIC designs and on millimeter-wave network analysis technologies. Since July 1992 he has been with Hughes Space and Communications Company, Los Angeles, CA. His current work involves III–V device characterization and the design of MIC's and MMIC's for microwave/millimeter-wave low-noise and power applications.

Eric Carman was born in Santa Barbara, CA, on August 30, 1965. He received the B.S.E.E. degree from California Polytechnic University, San Luis Obispo, CA, in 1989, and the M.S.E.E. degree from the University of California, Santa Barbara, in 1992.

He is now working on the development of smart power technologies at Motorola's Advanced Custom Technologies Group in Mesa, AZ.
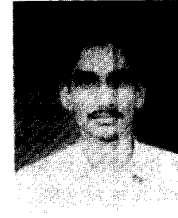
Rajasekhar Pullela was born in Hyderabad, India, on August 14, 1972. He received the B. Tech. degree in electronics and communication engineering from the Indian Institute of Technology, Madras, India, in 1993.

He is currently pursuing the M.S./Ph.D. degree in electrical engineering at the University of California, Santa Barbara. His current research involves diode and transistor circuits for high-speed fiber-optic applications.